A Ionospheric Measurement Techniques

A.1 Radio Wave Techniques in Ionospheric Physics

Rishbeth and Garriott (1969) describe the operation of ionosondes in some detail in their book, and we refer the reader to that source for information on that device. Ionosondes were the workhorse in ionospheric research for many decades and still are very useful instruments. Digital techniques have greatly improved their versatility and a new generation of "digisondes" is now in operation. We refer the reader to the paper by Wright and Pitteway (1979) for more information. In this section we discuss incoherent and coherent scatter radars and the radio wave scintillation technique. Further material may be found in articles by Fejer and Kelley (1980) and Farley (1979).

A.1.1 Incoherent Scatter Radars

The performance of radar and lidar systems (see Section A.2.2) is characterized by two expressions referred to as the radar and lidar equations. These equations tell the story of how energy is transmitted, scattered, and received. In each case, a large amount of energy is sent into the atmosphere, a small amount of the incident energy is scattered, and a smaller fraction of that scattered radiation finds its way back to the receiver. Both systems employ electromagnetic radiation but have evolved out of two quite separate research communities, each with its own vernacular. The radar scattering equation[1] has the form

$$P_r = \left(\frac{P_t G_t}{4\pi R^2} \right) (\sigma) \left(\frac{A_r}{R^2} \right)$$

Written in this form, the incoherent scatter radar equation tracks the progress of the radiation from transmission through to reception. (Note that σ here refers to a cross-section with units m^2.) Starting with the first term, if a pulse of power P_t

---

[1] Taken from the CEDAR Radar School notes, 1992 – Donald T. Farley.

was to originate from the mythical isotropic radiator, then at a distance R the power per unit area incident on a spherical shell is $P_t/4\pi R^2$. But radars are much more directional than an isotropic radiator by the factor G_t, the gain, and we arrive at the formula inside the first bracket. In the equation, $P_t G_t/4\pi R^2$ is thus the power delivered in each pulse per square meter into the region of interest. In the next two terms, σ is the backscattering cross section per unit solid angle [m^2], and A_t/R^2 is the solid angle of the receiving system.

The gain, G_t, of the main beam is inversely proportional to the solid angle illuminated by the antenna ($G_t = 4\pi/\Omega$). The beam solid angle, Ω, can be expressed for large antennas as $\Omega \approx \lambda^2/A_t$. If the transmitting antenna is equal to or larger than the receiving antenna and we lump all the efficiency factors into a single effective reception area, A_{eff}, the radar equation can then be simplified to

$$P_r = P_t \left(\frac{A_t A_{eff}}{\lambda^2 R^4} \right) \sigma$$

The backscattering cross section can be written as $\sigma = \eta V_s$ where η is the backscattering cross section per unit volume [m^2/m^3] and V_s is the scattering volume. (Note that here η is not the viscosity coefficient.) The volume term is of great interest when considering "soft" targets. If the scattering is from a missile, plane, satellite, and so on, it is termed a hard target. But in atmospheric scattering, the signal depends on the number of scatterers contained in the entire beam volume, which increases with increasing range. Written in terms of the solid angle, the scattering volume is $V_s \approx \Omega R^2 \Delta R$, where $\Delta R = c\tau_t/2$ (τ_r is the receiver bin time) defines the range resolution of the measurement. Remembering that $\Omega \approx \lambda^2/A_t$, the radar equation then takes the following form:

$$P_r = P_t \eta \Delta R \frac{A_{eff}}{R^2}$$

Notice that for a soft target the signal falls off as R^{-2}, rather than R^{-4} as might be guessed, due to the ever increasing size of the scattering volume with distance squared.

The ground was broken for the first incoherent scatter radar (ISR) site in Arecibo, Puerto Rico, in 1959. At the time of writing, there are 15 such sites. The locations of many of these sites are given in Table A.1 along with other relevant information. Data from most of these sites are used somewhere in the text. The Chatanika radar was moved to Sondre Stromfjord, Greenland, in 1983, and new facilities built in Alaska (PFISR) and in Resolute Bay, Nunavit, Canada, deep in the polar cap.

Like an ionosonde, an ISR transmits a radio wave signal and receives a returned "echo" sometime later. Ionosondes operate over frequencies typically in the

Table A.1 Relevant Parameters and Coordinates

Observatory	Frequency (MHz)	Geographic Latitude	Geographic Longitude	L	UT–LT
Jicamarca, Peru	49.9	11.9°S	76°W	1.05	5
Altair, Kwajalein	155.5	8.8°N	167.5°E	1.1	−11
MU, Japan	46.5	34.85°N	136.10°E	1.33	−9
Arecibo, Puerto Rico	430	18.3°N	66.75°W	1.43	4
St. Santin, France*	935	44.6°N	2.2°E	1.76	0
Millstone Hill, Massachusetts	440	42.6°N	71.5°W	3.12	5
Chatanika, Alaska*	1290	64.9°N	147.7°W	5.51	10
Poker Flat ISR (PFISR)	450	64.9°N	147.7°N	5.51	10
EISCAT (Tromso, Norway)	224/933	69.6°N	19.2°E	6.3	−2
Sondre Stromfjord, Greenland	1290	67.0°N	50.95°W	15+	3
EISCAT Svalbard Radar	500	78.1°N	15.1°E	20+	−1
Resolute Bay (Nunavit, Can.)**	450	75.0°N	95.0°E	100+	−6 hr

*Decommissioned; **Under construction.

range 1–20 MHz and rely on the fact that such a signal is reflected when its frequency, f, is equal to the local plasma frequency, f_p, where

$$f_p = (2\pi)^{-1} \left(ne^2/m_e\varepsilon_0 \right)^{1/2}$$

To a good approximation,

$$f_p = 9000\sqrt{n} \text{ Hz}$$

where n is the plasma density in reciprocal cubic centimeters. Since the peak plasma density in the ionosphere is a few times 10^6cm^{-3}, $f_p \leq 12$ MHz. Vertically transmitted frequencies above the peak plasma frequency in the overhead ionosphere go right through. Consequently, ground-based ionosondes yield no information above the height of the peak in the F region plasma density. If there is a dense E layer, it can block the F layer entirely. Occasionally, a thin low-altitude layer, such as the sporadic E layers discussed in Chapter 5, will allow some energy to tunnel through, revealing the F layer above.

The ISR technique circumvents both the reflection and topside problems by using frequencies well above any reasonable plasma frequency in the natural ionosphere. The lowest frequency listed in Table A.1 is about 50 MHz. Such waves are virtually unattenuated by the ionosphere and pass through almost unaffected into space. "Almost" is the key word here, since it is the small amount of energy scattered by the ionospheric electrons that is used by the ISR method. To gain some perspective, the amount of energy scattered back to a typical ISR antenna from 300 km is roughly comparable to the target represented by

a mm-diameter metallic sphere at the same range. It should be no surprise, then, that the largest of the ISR sites measure their effective power-aperture product in tens of megawatt-acres or in more reasonable units a few times 10^{11} W · m^2.

As with most radar systems, the signal is transmitted in pulses with range from the radar to the echoing region determined by dividing half the delay time by the speed of light. Since the ionosphere is an extended target, various ranges can be interrogated using the same set of pulses by analyzing the returned signal at appropriate time delays. The radar scattering equation is described in Section A.2.2.

The information in the returned signal is remarkably rich in physical content. The power in the returned echo is proportional to the number density of electrons in the volume irradiated. This stems from the fact that each electron incoherently radiates back a small amount of the incident energy. The electric field in the transmitted wave causes any and all electrons encountered during transit of the pulse to oscillate, resulting in radiation of a signal at almost the same frequency. This fact alone was sufficient to generate the enthusiasm necessary to build the first site at Arecibo because for the first time information on the ionosphere would be available above the F peak. The richness in information content stems as much from the spectrum of the returned signal as from the power returned, however. The electrons are consistently in thermal motion, and thus the radiation is Doppler shifted from the incident frequency. The result is a spread in the returned radio wave spectrum that contains considerable information about the velocities present in the medium and thus about its dynamics.

The original idea (Gordon, 1958) hypothesized quite naturally that the Doppler width of the returned spectrum would be of order

$$\delta f / f \cong \langle V \rangle_e / c$$

where $\langle V \rangle_e$ is the mean thermal electron velocity. Surprisingly, the first experiments, by Bowles (1958), showed the Doppler width to be of order $\langle V \rangle_i / c$, where $\langle V \rangle_i$ is the ion thermal speed. This is explained by the fact that, when the probing wavelength is greater than the Debye length, the electrons are linked to the ions through the Debye cloud around them, and part of the scattered signal (the ion line) is characterized by ion properties.

A schematic diagram of the Doppler spread due to scattering from thermal fluctuations in the so-called ion line is presented in Fig. A.1. The power under the curve is proportional to the number density, while the width δf can be used to determine the ion temperature. The relative intensity of the "wings" in the spectrum yields the electron temperature, and the overall shift of the spectrum, f_D, from the transmitted frequency f_T gives the line-of-sight component of the mean ion velocity $\mathbf{V}_i$. If several positions are used, the complete vector flow velocity can
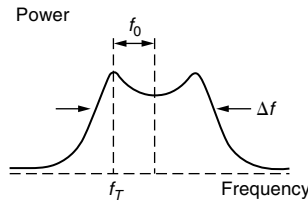
Figure A.1 Schematic diagram of the Doppler spectrum associated with backscatter from thermal fluctuation in the upper atmosphere. Here f_T is the transmitted frequency, f_0 is the mean Doppler shift, which yields the line-of-sight velocity, and Δf is a measure of the width of the spectrum. Only the ion line is shown here.

be found. In the F region the ion flow velocity yields the perpendicular electric field components via the relationship

$$\mathbf{E}_\perp = \mathbf{B} \times \mathbf{V}_i$$

The ion flow velocity parallel to **B** is much more complicated, since many factors contribute, such as the component of the neutral wind along **B**, the ion pressure gradient, and gravitational forces (see Chapter 2). The theory of scattering from thermal fluctuations is very well understood. In fact, as pointed out by Farley (1979), when viewed as a test of the crucial Landau damping method for carrying out Vlasov plasma theory, measurements of the incoherent scatter spectrum have verified that method to better than 1% accuracy. The radar scatters from irregularities in the medium, $\mathbf{k}_m$, according to the relationship

$$\mathbf{k}_T = \mathbf{k}_s + \mathbf{k}_m \tag{A.1}$$

where $\mathbf{k}_T$ is the transmitted wave and $\mathbf{k}_s$ the scattered wave. Since $\mathbf{k}_s = -\mathbf{k}_T$ for backscatter,

$$\mathbf{k}_m = 2\mathbf{k}_T$$

Thus, the scattering wavelength is one-half the transmitted wavelength. Equation (A.1) represents conservation of momentum since each photon carries a momentum equal to $\hbar \mathbf{k}$. Conservation of energy (each photon energy equal to $\hbar\omega$) requires

$$\omega_T = \omega_s + \omega_m \tag{A.2}$$

Thus, the Doppler width of the returned spectrum ($\omega_s - \omega_T$) is related to the frequencies of waves in the medium, ω_m. Since thermal fluctuations can be

considered as a superposition of damped sound waves, the spread in ω_m is of the order

$$\omega_m \approx |\mathbf{k}_m| C_s$$

where C_s is the sound speed in a plasma,

$$C_s^2 = (kT_e + kT_i)/M_i$$

The width of the ion line for a 50 MHz radar in a plasma with $C_s \approx 1000$ m/s is thus of order $[(4\pi/6)\,\text{m}](1000\,\text{m/s}) \approx 4000\,\text{rad/s} \approx 600\,\text{Hz}$. For a medium of the same temperature the Doppler width will just scale with the radar frequency, so at Arecibo (430 MHz) the width of the "ion line" is about eight times larger.

The peaks or wings in the ion line spectrum correspond to the frequency of the normal modes in the medium, that is, the frequency at which a finite-amplitude sinusoidal sound wave of wave number $\pm\mathbf{k}_m$ would exist. In thermal equilibrium such waves are damped. The time dependence associated with this damping fills in the remainder of the spectrum above and below $|\omega_s| = |\mathbf{k}_m| C_s$. When $T_e/T_i > 1$, Vlasov theory predicts that the sound wave damping will be less. Indeed, as mentioned above, these wings increase in amplitude relative to the rest of the spectrum when T_e/T_i increases. However, the total power decreases in this case by the factor $2/[1 + (T_e/T_i)]$.

In ion sound waves, both electrons and ions participate. The electron gas can itself support thermal fluctuations, which at the scattering wave number occur at frequencies of order $k_m <V>_e$. This frequency is larger by a factor M_i/m_e than the frequency of the wings in the ion line. In the ionosphere for O^+ this ratio is about 3×10^4, so the pure electron waves are Doppler shifted considerably more. The first simultaneous observations of both ion and electron scattering lines (called plasma lines) are reproduced in Fig. A.2a. The data were taken in the altitude range 1460–2486 km over Arecibo, where H^+ is the dominant ion. Figure A.2b shows both the plasma and the gyro lines as a function of time near 200 km. The latter is an electrostatic wave in a magnetized plasma that also exists in thermal equilibrium related to the whistler mode electromagnetic branch.

In practice, most ISR systems measure the temporal autocorrelation function of the signals scattered from a fixed point in space by sending up a series of pulses. Since the spectrum is the Fourier transform of the autocorrelation function (ACF), it can be generated at will on the ground using the latter. The temporal resolution is then determined by how many such measurements must be averaged to generate a reasonable ACF. Since the theory is exact, least-squares fitting methods can be used on the ACF waveform which include second-order ion species, differential drifts of the various ions, and so forth. This further increases the information on the ionosphere available via the ISR method.
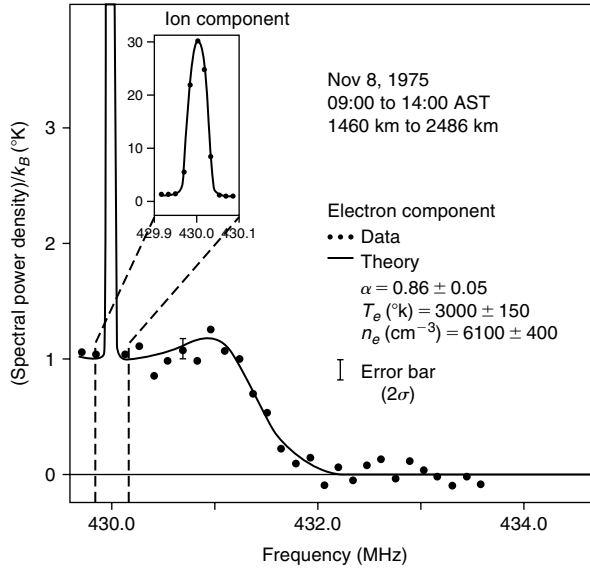
Figure A.2a   Incoherent scatter data from the ionosphere at Arecibo showing, for the first time, the electronic as well as ionic portions of the spectrum. Due to the wide bandwidth and resulting low signal-to-noise ratio, a great deal of averaging in both time and space is required. [After Hagen and Behnke (1976). Reproduced with permission of the American Geophysical Union.]
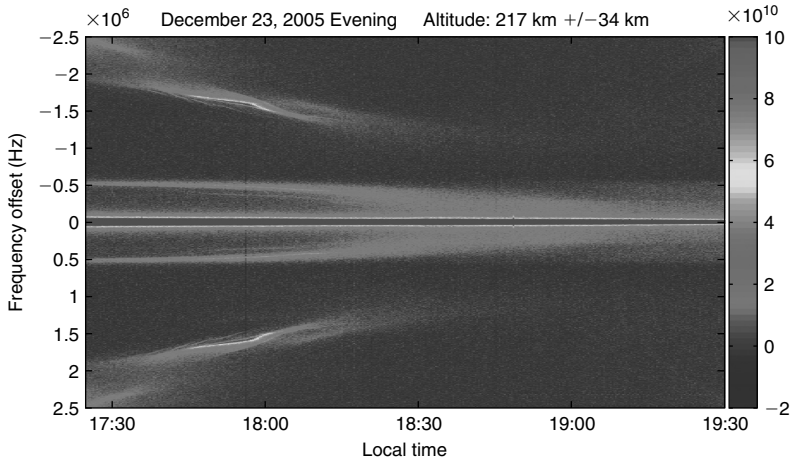
Figure A.2b   Up- and down-shifted plasma and gyroline measurements at -217 ± 34 km as a function of time using the Arecibo radar. The gyroline is a 0.5 MHz at 1730 and decreases with time. Notice the split in the higher-frequency plasma line. (Figure courtesy of A. Bhatt.)
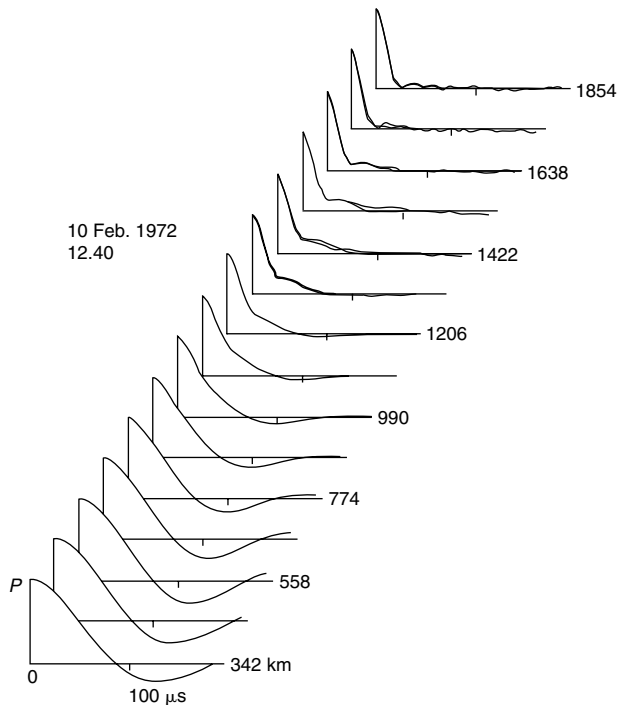
Figure A.3   Incoherent scatter autocorrelation function measurements of the ion line made at Arecibo. The pulse length used was 2 ms and the integration time was 20 min. The experimental and fitted theoretical curves are plotted together, but the agreement is so good that the two often cannot be distinguished. [After Hagen and Hsu (1974). Reproduced with permission of the American Geophysical Union.]

Examples of ACF measurements are presented in Fig. A.3 as a function of altitude over Arecibo. The fitted theoretical ACFs are superposed on the measurements and can hardly be distinguished. Notice that, as the altitude increases, the ACF narrows in time, corresponding to the widening of the Doppler spectrum as the plasma changes from O^+ to H^+ with increasing altitude.

A.1.2   Coherent Scatter Radars

When plasma instabilities are present in the ionosphere, the amplitude of fluctuations in the medium can grow to values much greater than the thermal level. If the wave number of these fluctuations matches the requirement in Eq. (A.1), then smaller radar systems can be used to detect these large fluctuations. The Doppler spectrum in such a case is then representative of the phase velocity of the non-thermal waves rather than of the bulk motion and temperature of the plasma. Of course, a large ISR system will also detect such waves if they are present.

The CEIS/ESF maps made using the Jicamarca ISR system and presented in Chapter 4 are of this type. Signal strengths more than 60 dB above the thermal fluctuation level have been recorded there.

Most of the plasma instabilities detected by coherent scatter radars (CSRs) produce waves with **k** vectors nearly perpendicular to the magnetic field. At the magnetic equator the plane perpendicular to **B** includes the vertical direction. Thus, coherent scattering can (and does) occur at all elevations in that plane. The large antenna at Jicamarca can be oriented only a few degrees off vertical but smaller steerable antennas are used to look obliquely east or west to study electrojet and spread F instabilities. It is quite easy to keep the beam perpendicular to **B** in the equatorial case.

At higher latitudes the perpendicularity requirement places a severe constraint on the location of the radar system and its field of view. To study instabilities in the auroral electrojet at, say, 110 km, the radar must be located many hundreds of kilometers south of the region of interest. An example of the "aspect" angle contours for a CSR radar located in Ithaca, New York (42.3°N, 75.4°E), is shown in Fig. A.4a. The L shell is also plotted in that figure and in Fig. A.4b, which shows the geographic location. The angle α is near 90° over a broad range of L shells and geographic distance. Linear theory predicts that echoes should occur only for aspect angles within a few degrees of perpendicularity. However, experiments show that during conditions of strong auroral activity, echoes are seen up to 8° off perpendicular. Although
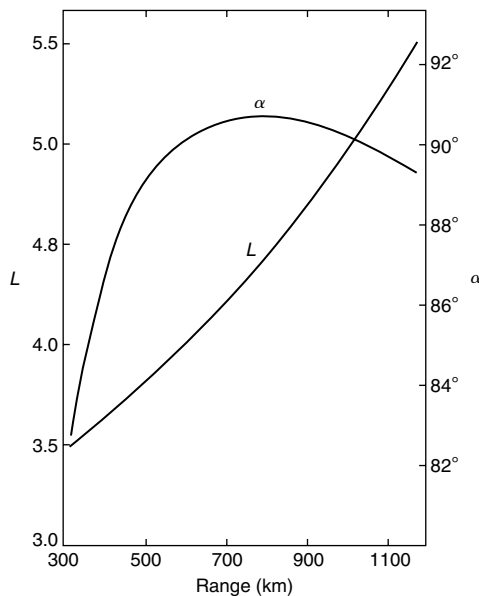

Figure A.4a L values and aspect angle for altitude 110 km along the Ithaca radar beam.
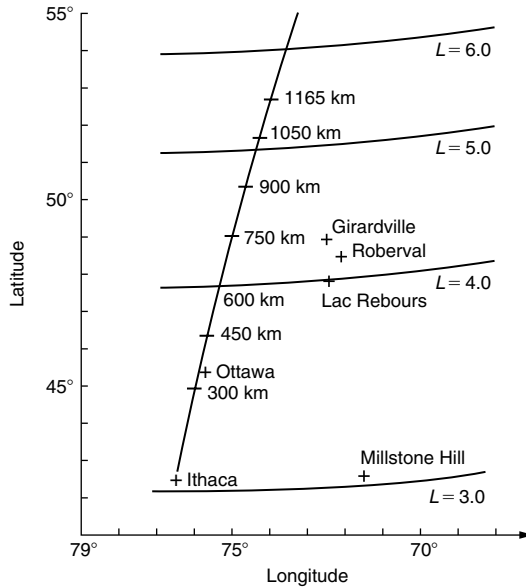
Figure A.4b   Location of the Ithaca auroral radar and its bearing.

not completely understood theoretically, this is very fortunate from the exper-
imental viewpoint since (a) the total range over which echoes are received
increases and (b) locations thought to be inaccessible to the technique are actu-
ally feasible. For example, although the nearly vertical magnetic field condi-
tions in Greenland yield poor aspect angles, strong echoes were received over
Sondre Stromfjord, Greenland, by a 50 MHz radar located at the southern tip
of Greenland.

Most CSR success has been at VHF and UHF frequencies. In CEIS, coherent
echoes have been found at wavelengths of 3 m, 0.95 m, 0.37 m, and even 0.11 m
(scattering) during extreme conditions. Equatorial electrojet measurements at
lower frequencies (larger scattering wavelengths) have been made occasionally
at Jicamarca and quite extensively in Africa (Hanuise and Crochet, 1978). These
so-called HF radars suffer more refraction and the echoing mechanism is some-
times ambiguous due to the proximity of the frequency to ambient plasma fre-
quencies. That is, it is not always clear whether the system is operating as a
radar or more like a classical ionosonde. At very high latitudes the refractive
properties at HF can actually be an advantage since, as just noted, it is not easy
to obtain the line-of-sight aspect angles perpendicular to **B** needed by VHF sys-
tems. A rotating HF system was used near the magnetic dip pole, for example,
to yield nearly uniform coverage in azimuth since the refraction relative to a ver-
tical magnetic field line yielded identical aspect angles at all azimuths (Tsunoda
et al., 1976).

   The latter HF technique is particularly useful in the summer, when the polar cap is illuminated by sunlight and refraction occurs virtually all day long. At this point it is worth reiterating that all radar scattering is proportional to $\delta n(\mathbf{k}_s)$, not to $\delta n(\mathbf{k}_s)/n_0$. That is, electrostatic plasma waves which have the same $(\delta n/n_0)$ amplitude will scatter more strongly at high background density levels than at low ones for the same amplitude wave. For this reason the daytime equatorial electrojet can be detected with low-power systems—for example, some tens of kilowatts—but nighttime echoes are much harder to get even though the plasma waves are just as intense. The Doppler shift of the returned signal is not nearly so straightforward to interpret as is that from an incoherently scattered signal since the phase velocity of the waves depends on the plasma physics of the process creating the waves. Figure A.5 shows an interferometric image of the scattering volume in a sporadic E event over Puerto Rico. The alignment of these scattering centers is related to quasiperiodic echoes.

   A method has been developed by Farley and co-workers to track the location of strong scattering regions across the coherent scatter radar field of view. Two antennas are used, separated by a known distance in, say, the east (E)-west (W) direction, and the complex cross spectrum is determined:

$$S_{EW}(\omega) = \frac{\left\langle F_E(\omega)F_w^*(\omega)\right\rangle}{\left\langle |F_E(\omega)|^2\right\rangle^{1/2}\left\langle |F_W(\omega)|^2\right\rangle^{1/2}} \tag{A.3}$$

where $F(\omega)$ is the Fourier transform of the digitized signals from the respective antennas. For each line-of-sight Doppler frequency the magnitude of $S_{EW}(\omega)$ is
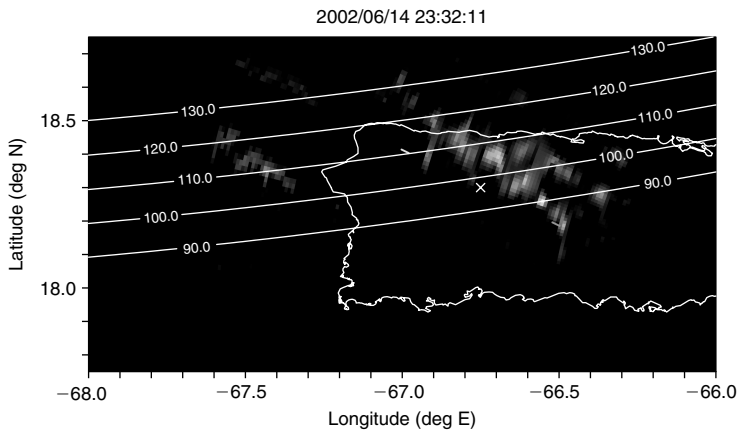
Figure A.5   Radar image of coherent echoes received at 23:32 UT. Note that UT $=$ LT $+$ 4. Blue corresponds to echo velocity toward the southeast and yellow-green toward the northwest. [After Hysell et al. (2004). Reproduced with permission of the European Geosciences Union.]

the normalized coherence of the scatterer. When the coherence is high in some frequency band, it means that the scatterer is localized within the beamwidth. In such a case, the phase angle ϕ of the complex number $S_{EW}(\omega)$ determines the position of the scatterer within the beam. As ϕ changes in time, the scatterer can be tracked across the field of view and its cross velocity therefore determined. In some cases this velocity is very likely equal to the plasma flow velocity [e.g., the equatorial F region case studied by Kudeki et al. (1981)]. In the E region the method yields the phase velocity of the large-scale waves which dominate the physics. In some sense the two situations are equivalent; the large-scale F region waves move with the plasma flow, so the interferometer in both cases measures the "phase velocity" of the large features that are creating conditions conducive to generation of the 3-m waves that scatter the 50 MHz waves. The technique has also been used in the auroral zone (Providakes et al., 1983; Bahcivan et al., 2005). Note that if the two antennas are separated north-south, the vertical position of the scattering centers may be found. This has considerable potential for auroral physics since it is not yet entirely clear at what height the scattering takes place.

A.1.3   Scintillation Techniques

The scintillation method is used to study the ionosphere by measuring the fluctuations of a radio signal due to its traversal through an irregular medium. In this method, the medium is considered to be equivalent to a diffracting screen with random density irregularities which are frozen in the uniform background and move with a fixed velocity. It is assumed that absorption by the medium is negligible. If the diffracting region is thin, the variations in the emerging wave front are present only in the phase and not in the amplitude of the signal. As the wave propagates beyond the screen, fluctuations in amplitude begin to develop, due to interference effects. This approach was initially used in a number of limiting cases by Hewish (1952) and Wagner (1962), who considered a one-dimensional thin screen; by Bowhill (1961) and Mercier (1962), who considered a two-dimensional thin screen; and by Tatarskii (1961) and Budden (1965), who generalized these studies by assuming a two-dimensional thick screen. These limiting cases were reviewed by Salpeter (1967), who extended the theory to important regimes which had not been previously considered, derived sufficient conditions for the validity of the "thin phase screen" approximation, and investigated the effect of a finite angular source size on the scintillation spectrum for any regime. It was found that, under the weak-scattering, thin-screen approximation, the power spectrum of the density fluctuations must be multiplied by a function that depends on the height of the irregularity layer and on the frequency of the incident wave to yield the power spectrum of the observed scintillation. That is, the power spectrum of the scintillation is a linearly filtered version of the power spectrum of the density fluctuations, under these

approximations. The multiplying function, known as the Fresnel filtering factor, acts as a high-pass filter and has deep minima at points which are proportional to the square root of integer numbers (Bowhill, 1961; Budden, 1965; Salpeter, 1967). These minima are smeared when the irregularity layer is thick (Tatarskii, 1961; Budden, 1965), but when they are present in the scintillation power spectrum, they provide information that can be used to estimate the velocity of the medium (Lovelace et al., 1970; Rufenach, 1972).

A crucial step in the theory of scintillation is the choice of a model for the power spectrum of the density irregularities. Prior to about 1970, all the authors assumed a Gaussian spectrum for both interplanetary and ionospheric irregularities. A Gaussian description is mathematically convenient and in the absence of further information was thought to be a reasonable representation. Many scintillation observations were then used to infer "dominant" density scales, both for the interplanetary medium and for the F region ionosphere, which were several orders of magnitude smaller than the directly observed outer scale dimensions. In addition, calculated scintillation levels based on Gaussian irregularities could not explain the unexpectedly large scintillation levels reported at UHF and higher frequencies.

Since the results of in situ measurements of density fluctuations in both the interplanetary space and the ionosphere can be interpreted in terms of a power law spectrum, this shape has been assumed by several authors in the study of interplanetary (Cronyn, 1970; Lovelace et al., 1970) and ionospheric scintillation (Rufenach, 1971, 1972, 1975). Rufenach (1975) derived approximate expressions, which were subsequently determined exactly by Costa and Kelley (1977), that show that the scintillation levels based on power law irregularities are larger than those based on Gaussian irregularities for similar rms density fluctuation levels.

In the weak-scattering, thin-screen approximation, the medium is replaced by a plane surface along which the phase of the radio wave fluctuates but the amplitude remains constant. As the wave propagates beyond the screen, fluctuations in amplitude begin to develop, due to interference effects. Let $P_\phi(k_x, k_y)$ be the power spectrum of the phase fluctuations in the wave emerging from an irregularity layer and $P_I(k_x, k_y)$ be the power spectrum of the intensity fluctuations in the received signal, expressed in a reference frame with the k_z axis aligned with the direction of the incident wave. It has been shown (Bowhill, 1961; Rufenach, 1975; Salpeter, 1967) that the following relations apply in the weak-scattering limit:

$$P_\phi\left(k_x, k_y\right) = 2\pi(r_e\lambda)^2(L\sec\psi)P_N\left(k_x, k_y, k_z = 0\right) \tag{A.4}$$

and

$$P_I\left(k_x, k_y\right) = 4\sin^2\left[\left(k_x^2 + k_y^2\right)\Big/k_f^2\right]P_\phi\left(k_x, k_y\right) \tag{A.5}$$

where $k_f^2 = 4\pi/Lz$, λ is the wavelength of the incident wave, z is the distance (measured along the ray path) from the source to the observation point, ψ is the angle between the ray path and the vertical at the point where the ray path intercepts the phase screen, r_e is the classical electron radius ($r_e = 2.82 \times 10^{-15}$ m), L is the thickness of the irregularity layer, and $P_N(k_x, k_y, k_z = 0)$ is the two-dimensional wave number power spectrum in the electron density fluctuations in the plane perpendicular to the $\mathbf{k}$ vector of the incident radio wave.

Scintillation measurements of P_ϕ and P_I thus yield information on the two-dimensional wave number spectrum of electron density fluctuations in the ionospheric plasma. These in turn can be compared to one-dimensional measurements of electron density fluctuations made by probes flown on rockets or satellites, which are related to $P_N(\mathbf{k})$ by

$$P_{ID}(k_x) = \iint P_N(\mathbf{k}) dk_y dk_z$$

where the x-axis is taken along the direction of travel. In the case of power law irregularities, one important effect of the integration performed by the spacecraft measurement is to decrease the slope of the power law by one unit relative to the phase spectrum P_ϕ. That is, a phase spectrum which varies as k^{-3} corresponds to a one-dimensional in situ spectrum which varies as k^{-2}. It is also clear from (A.4) and (A.5) that phase scintillation measurements are more closely related mathematically to the in situ fluctuations since the Fresnel factor, $\sin^2[(k_x^2 + k_y^2)/k_f^2]$, does not appear. Most recent measurements use P_ϕ, and considerable effort has gone into dedicated beacon experiments on satellites which radiate a number of frequencies all in phase with a high-frequency carrier (e.g., the *Wideband* and *HILAT* satellites).

Scintillations of signals from a rapidly moving low-altitude satellite beacon yield a rapid cut across an irregular region. The phase scintillation level will then vary in time as the satellite beam traverses different plasma regions. The *frequency* spectrum of the measured phase scintillations thus yields a measure of the in situ *wave number* power spectrum. Likewise, an airplane-based measurement system can use signals from a high-altitude satellite (with a very slow angular velocity across the region of interest) using the aircraft velocity to map out an in situ irregularity spectrum. A fixed ground site will also receive time-varying phase scintillations from a high-altitude satellite as a structured medium passes overhead. If that velocity is known the in situ spectrum can be determined. If several "spaced" receivers are used, correlation methods can in principle be used to determine the velocity of the medium as it passes over the site.

The Global Positioning System was designed to avoid scintillations by going to frequencies above 1 GHz. However, during even modest equatorial convective storms, scintillations still create problems.
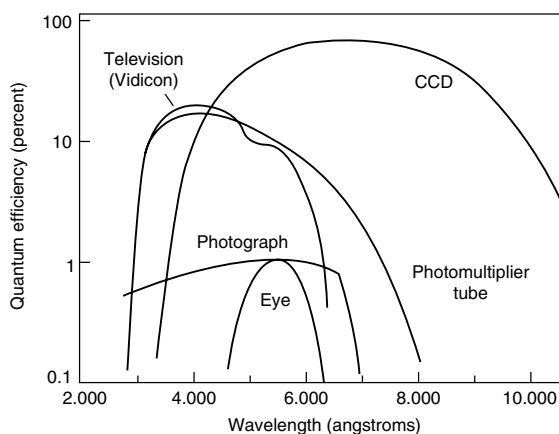
A.2   Optical Methods

A variety of passive and active optical methods exist for aeronomical studies. Aurora can be detected with the naked eye, as can noctilucent clouds, long-lived meteor trails, and intense mesospheric bores. Figure A.6a shows the wavelength coverage of various methods.

A.2.1   Airglow

The earth's airglow is faint and cannot readily be seen with the human eye (particularly because the strongest airglow emission lies outside the range of the human eye, in the near infrared (e.g., Wayne, 1991). Still, using sensitive optical equipment (e.g., photometers or, in our case, CCD imagers), the airglow can be detected and measured in the night sky. It is also possible to study airglow from space at wavelengths not overwhelmed by reflected sunlight, or even during the day using interferometric techniques. The latter is quite difficult due to the overwhelming background of sunlight, and we cannot yet do such studies with an airglow imager.

Airglow intensity is measured in flux of photons per unit area per second. The standard unit of measure is the Rayleigh which corresponds to 10^6 photons/cm$^2\cdot$s and is named in honor of Robert John Strutt, the fourth Lord Rayleigh (the term "Rayleigh Scattering" is named in honor of his father, the third Lord Rayleigh). The Rayleigh unit is convenient for airglow because of its relationship with the volume emission rate V. V is defined as the emission per unit volume per unit time in photons/cm^3/s, and is given by:

$$V = k_r \left[A^* \right] \tag{A.6}$$

Figure A.6a   Quantum efficiency of various optical methods. Six thousand angstroms equals 600 nm. (Figure courtesy of J. Makela.)

where k_r is the rate coefficient, and $[A^*]$ is the concentration of the excited chemical specie A. k_r is equivalent to the transition probability and is related to the radiative lifetime, τ, by:

$$\tau = \ln 2 / k_r \tag{A.7}$$

The observed intensity, I (in Rayleighs) is related to the volume emission rate, V, according to:

$$I = 10^{-6} \int V(z) dz \tag{A.8}$$

As atmospheric disturbances such as acoustic gravity waves pass through an airglow layer, they cause perturbations in the density of the relevant constituent ($[A^*]$), and/or in the rate coefficient (k_r) of the relevant reaction (which are temperature dependent), and in turn cause intensity variations according to (A.6) and (A.7). It is through these intensity variations that we are able to study the disturbances. The reader is referred to Wayne (1991) and Rishbeth and Garriott (1969) for a more detailed investigation of the chemistry.

The brightest of the airglow emissions are the NIR hydroxyl (OH), the 557.7 nm (O^1S) and the 630.0 nm (O^1D), and the emissions from metallic atoms, including sodium, calcium, potassium, and magnesium. The OH and 557.7 emissions come about due to reactions involving neutral species. They originate in the MLT region where the chemistry is dominated by the neutrals but where the density is not so great as to quench the emissions. In comparison the 630.0 reaction involves ion chemistry and so occurs much higher, where the atmosphere has a plasma embedded in it. The 630.0 emission chemistry is accompanied by a weak 557.7 airglow so care must be taken in interpreting the latter with a purely MLT source. Similarly, one of the OH bands falls near our 630.0 filter passband [at 625.8 nm corresponding to the (9,3) OH transition]. The 777.4 emission comes from recombination of atom oxygen.

Figure A.6b shows an illustration depicting the heights of several airglow layers. The full width at half maximum (FWHM) of the mesospheric layers is generally on the order of about 10 km, whereas for the 630.0 and 777.4 nm emissions in the thermosphere it is about 100 km (Baker and Stair, 1988). We cannot independently determine the height from our integrated measurement, but numerous rocket experiments have verified the illustration in Fig. A.6b. In the rest of this section we will give a general overview of the chemistry involved for these airglow emissions.
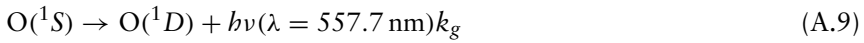
The 557.7 nm Emission

The green line emission was one of the first airglow emissions to be discovered and, as far back as 1923 (Bates, 1981) it was known that the emission is due to
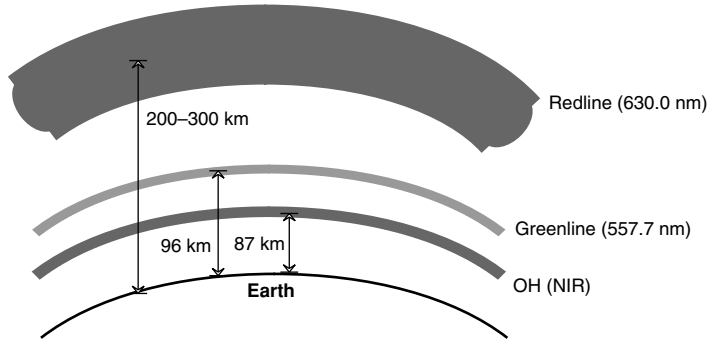
Figure A.6b Illustration of the heights of the different airglow layers, along with the wavelengths of the emissions. (Not to scale.)

the transition:

$$O(^1S) \rightarrow O(^1D) + h\nu(\lambda = 557.7\,\text{nm})k_g \tag{A.9}$$

Since the preceding transition results in atomic oxygen in the $O(^1D)$ state, one might expect a 5577 emission to be immediately followed by a 6300 emission because the 6300 emission comes from the $O(^1D)$ state (see the next section). The reason this does not occur is due to the long lifetime of the $O(^1D)$ state (110 s) (Rishbeth and Garriot, 1969). At the height of the 5577 emission, collisions are so frequent that the $O(^1D)$ state is deactivated well before it can radiate a red photon.

The source of the excited $O(^1S)$ is now generally accepted to be the two-step Barth mechanism, given by

$$O + O \xrightarrow{M} O_2^* \quad \alpha_1 \tag{A.10}$$

$$O + O_2^* \rightarrow O\left(^1S\right) + O_2 \quad \beta_1 \tag{A.11}$$

which requires a collision with a third-body M (most probably N_2). The rate coefficients are given by k_g, α_1, and β_1.

There are also competing processes for loss of O_2^* in the form of deactivation and direct emission:

$$O_2^* + M \rightarrow O_2 + M \quad \beta_2 \tag{A.12}$$

$$O_2^* \rightarrow O^2 + h\nu \quad \beta_3 \tag{A.13}$$

Equating terms for production and loss of O_2^* we have

$$\alpha_1[O]^2[M] = \beta_1 \cdot [O_2^*][O] + \beta_2 \cdot [O_2^*][M] + \beta_3[O_2^*] \tag{A.14}$$

Solving for the rate of production of $O(^1S)$ we have

$$[O_2^*][O]\beta_1 = \frac{\alpha_1\beta_1[O]^3[M]}{\beta_1[O] + \beta_2[M] + \beta_3} \tag{A.15}$$

From (A.6) and (A.15) we can solve for the total emission rate of the 557.7 nm emission in terms of the various species concentrations and reaction rates [assuming that the only loss of the $O(^1S)$ state is emission]:

$$I = 10^{-6}k_g = \frac{\alpha_1\beta_1[O]^3[M]}{\beta_1[O] + \beta_2[M] + \beta_3} \tag{A.16}$$

Assuming that $\beta_2[M] \gg \beta_2[O]$, β_3, we have

$$I = 10^{-6}k_g \cdot \frac{\alpha_1\beta_1}{\beta_2}[O]^3 \tag{A.17}$$

And so the emission rate is proportional to the cube of the concentration of atomic oxygen. Figure A.7 plots this function using data from the MSIS-86 model. The bulk of the concentration of O lies between 95 km and 100 km and therefore explains the origin of the emission as a layer. Indeed, during the
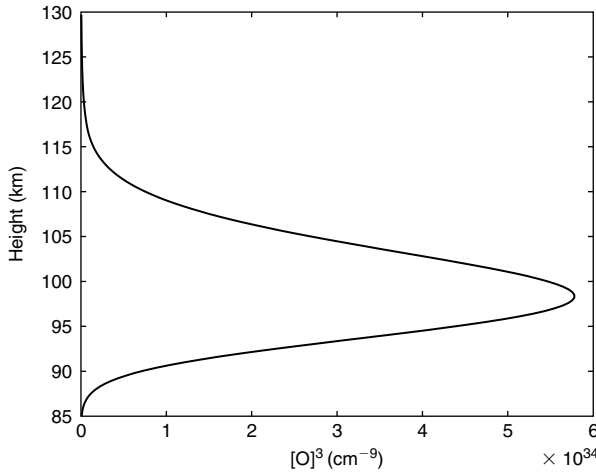
Figure A.7   Atomic oxygen profile as generated by the MSIS-86 model for the geographic latitude and longitude of Arecibo, Puerto Rico.

ALOHA-93 campaign, two all-sky imagers were used to triangulate the height of the 557.7 nm emission structures. The height was found to be 95 ± 2 km (Taylor et al., 1995).

The NIR OH Broadband Emission

The hydroxyl is the brightest of the nighttime emissions. The light is generated from a series of transitions between rotational and vibrational states (rather than a single transition between electrical states), which generate light at multiple frequencies and constitutes a broadband emission process.

The vibrationally excited OH species arise from a reaction involving atomic hydrogen and ozone:

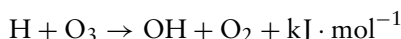$$H + O_3 \rightarrow OH + O_2 + kJ \cdot mol^{-1}$$

Figure A.8a shows a graph of the relative intensities of the different OH lines from 725.1 nm to 896.2 nm, and Table A.2 lists them along with the transitions that generate them. These are the values as computed by Meinel (1950), who first identified OH in the airglow spectrum. The OH emission bands subsequently became known as the *Meinel Bands* in honor of this scientist.

There exists an O_2 band centered at 864.6 nm that lies in the heart of this region, which is why the OH filters that are used for the imaging have a notch to suppress this emission (Swenson and Mendi, 1994). Another interesting fact pointed out by Meinel is the existence of an OH line at 625.8 nm, in the visible spectrum. This line is close to the 630.0 nm, which leads to the possibility of some OH contamination of thermospheric images. Figure A.8b shows images taken with both the 6300 and OH filters showing this effect. The two brightest bands in the OH image are faintly visible in the 6300 image. The high OH intensity must have been enough to leak through the sidelobes of the 2 nm passband for the 630.0 nm filter. The bands were also faintly visible in a 1 second exposure taken with no filter, but not in the 90 second background image (at 541 nm).
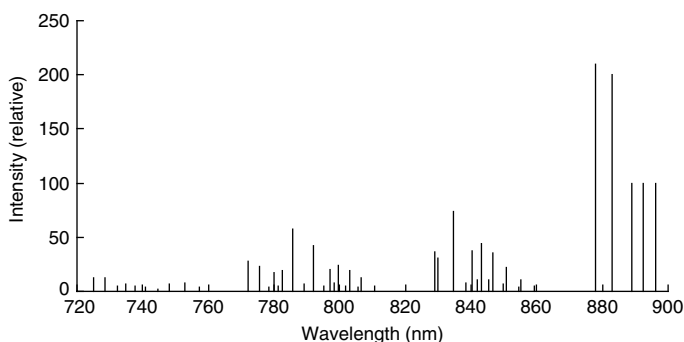

Figure A.8a   The relative intensities of the different OH lines.

Table A.2 Wavelengths, Intensities, and Transitions for the Different OH Lines in the 725 nm–897 nm Range (Meinel, 1950)

λ(nm)	I	(v', v'')RQP	λ(nm)	I	(v', v'')RQP
725.1	12	(8,3)R	829.0	36	(6,2)R
728.4	12	(8,3)Q	830.0	31	(6,2)R
732.3	5	(8,3)P_1	834.7	74	(6,2)Q
734.8	7	(8,3)P_2	838.5	8	(6,2)p_1
737.6	5	(8,3)P_3	840.2	37	(6,2)P_1
740.8	4	(8,3)P_4	841.8	11	(6,2)p_2
744.5	2	(8,3)P_5	843.2	44	(6,2)P_2
748.2	7	(4,0)R	845.5	11	(6,2)p_3
752.9	8	(4,0)Q	846.7	35	(6,2)P_3
757.2	4	(4,0)P_1	849.7	7	(6,2)p_4
772.0	28	(9,4)R	850.7	22	(6,2)P_4
775.6	23	(9,4)Q	854.5	4	(6,2)p_5
778.3	4	(9,4)p_1	855.1	11	(6,2)P_5
779.9	17	(9,4)P_1	859.4	5	(6,2)P_6
781.4	5	(9,4)p_2	877.8	~210	(7,3)R
782.6	19	(9,4)P_2	882.9	~200	(7,3)Q
785.8	57	(9,4)P_3	888.9	~100	(7,3)P_1
787.4	–	(5,1)R	892.4	~100	(7,3)P_2
789.3	7	(9,4)P_4	896.2	~100	(7,3)P_3

OH 05:12:26 AST   6300 05:12:22 AST
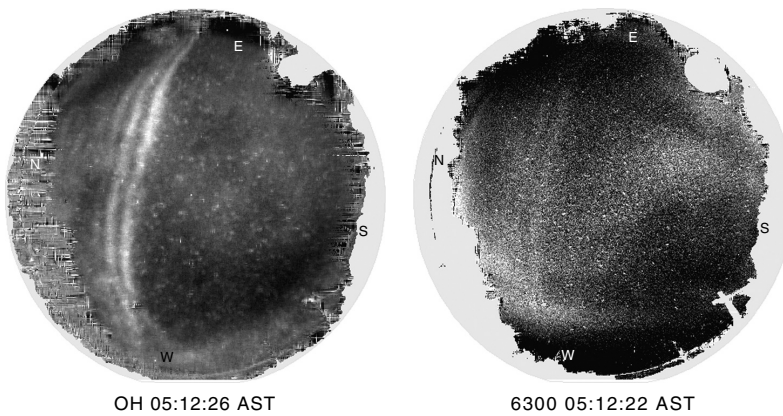
Figure A.8b   Images showing contamination of OH emission into the 6300 filter image. Also note that the structure is a mesospheric bore (see Chapter 7).

The OH chemistry is complicated by the fact that there are so many transitions involved. Swenson and Gardner (1998) have developed a model for calculating the volume emission rate of the OH(8,3) transition at $\sim$737 nm. The result is dependent upon the concentrations of O, O_2, and N_2, though they make the assumption that $[N_2] = 3.54[O_2]$. The equation they derived is

$$V(8, 3) = \frac{K_1[O][O_2]^2(200/T)^{2.5}}{1 + K_2[O_2]} \tag{A.19}$$

where $K_1 = 8.25 \times 10^{-36} \, \text{cm}^6 \, \text{s}^{-1}$ and $K_2 = 7.7 \times 10^{-14} \, \text{cm}^3$.

According to the MSIS-90 the neutral densities are given by

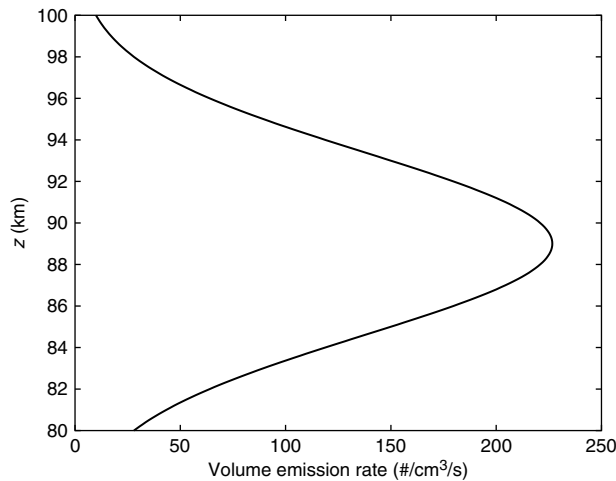$$[O] = 1.2 \times 10^{12} \text{cm}^{-3} \exp[-(z - z_0)/H_0 - e^{-(z-z_0)/H_0}] \tag{A.20}$$

where $z_0 \approx 98$ km and $H_0 \approx 8.7$ km, and

$$[O_2] = 3.45 \times 10^{12} \, \text{cm}^{-3} e^{-(z-z_0/H)} \tag{A.21}$$

where $H \approx 6$ km. Assuming $T = 200$ K, this results in the following formula for the volume emission rate:

$$V = \frac{120 \exp\left[-(z - z_0)\left(\frac{2}{H} + \frac{1}{H}\right) - e^{-(z-z_0)/H_0}\right]}{1 + 0.27e^{-(z-z_0)/H}} \tag{A.22}$$

A plot of this equation is shown in Fig. A.9. The height of the peak of the emission rate is at 89 km, which is above the mean height of 87 km that rocket-borne


Figure A.9 OH volume emission rate vs. height. (Figure courtesy of Jonathan Makela.)

experiments have shown (Baker and Stair, 1988). The FWHM is approximately 10 km, which is also larger than the rocket experiments indicate.

The 630.0 nm Emission

The 630.0 nm emission is an effective although complicated tracer for the dynamics of the ionosphere near the peak of the F region (250–300 km). Its volume emission rate is dependent on both the electron density and the neutral O_2 density, and so its peak emission altitude follows the rise and fall of the F layer, with the peak emission altitude in general lying *below* the F peak. Furthermore, the emission intensity drops off dramatically with altitude if the F layer rises. This effect is easily confused with decreasing intensity due to a drop in electron content.

The 630.0 nm emission arises from the transition:

$$O(^1D) \rightarrow O(^3P) + h\nu(\lambda = 630.0 \, \text{nm}) \tag{A.23}$$
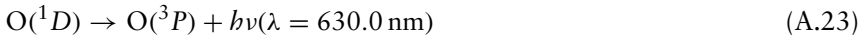
The $O(^1D)$ state is populated by dissociative recombination of O_2^+, which itself arises from a collisional charge transfer between neutral molecular oxygen and ionized atomic oxygen.

$$O^+ + O_2 \rightarrow O_2^* + O \quad k_1$$
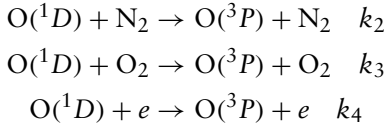$$O_2^+ + e \rightarrow O(^1D) + O(^3P) + 4.49 \, \text{eV} \quad \alpha$$
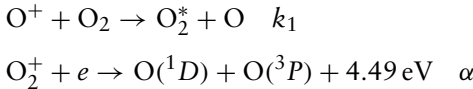
It is also possible for dissociative recombination to produce oxygen in the $O(^1S)$, but experimentally it has been shown that it is a small fraction ($\sim15\%$) of the $O(^1D)$, so it has generally been ignored as a source for $O(^1S)$ (Rishbeth and Garriott, 1969). With the CU Imager, however, we have seen that the thermospheric contribution to the $O(^1S)$ state can be considerable when electron densities are high. Figure A.10 shows raw images taken with the 557.7, 630.0, and background filters the night of February 17, 1998.

5577 22:03:39   6300 22:07:01   BGND 22:05:18
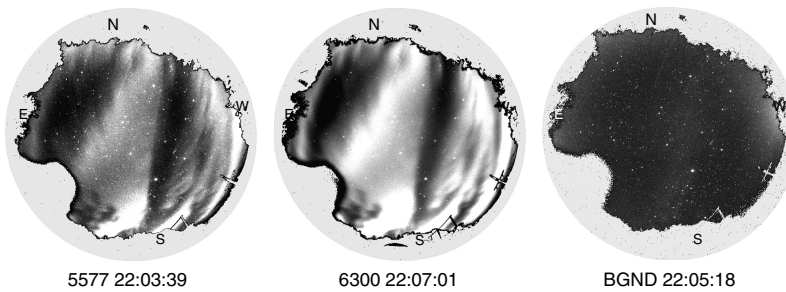
Figure A.10   Images showing thermospheric contribution to the 557.7 nm emission. The figure labels are in angstroms.

The competing reactions for the loss of the $O(^1D)$ state arise from collisions with N_2, O_2, and free electrons.

$$O(^1D) + N_2 \rightarrow O(^3P) + N_2 \quad k_2$$
$$O(^1D) + O_2 \rightarrow O(^3P) + O_2 \quad k_3$$
$$O(^1D) + e \rightarrow O(^3P) + e \quad k_4$$

The volume emission rate is then given by

$$V_{630.0} = \frac{\beta A_{630.0}\alpha[O_2^+][e]}{A_{630.0} + A_{636.4} + k_2[N_2] + k_3[O_2] + k_4[e]} \tag{A.24}$$

$A_{630.0}$ and $A_{636.4}$ are the Einstein transition coefficients for the 630.0 nm and its doublet at 636.4 nm. β is the production efficiency of the $O(^1D)$ state by the dissociative recombination reaction. Equating the production and loss of O_2^+,

$$\alpha[O_2^+][e] = k_1[O^+][O_2] \tag{A.25}$$

results in:

$$V_{630.0} = \frac{\beta A_{630.0}k_1[O^+][O_2]}{A_{630.0} + A_{636.4} + k_2[N_2] + k_3[O_2] + k_4[e]} \tag{A.26}$$

which is equivalent to the one quoted by Miller (1996).

To generate a height profile of the volume emission rate, we will use the values given in Table A.3 for the constants in (A.26). The reaction rate coefficients are functions of temperature, and so the values quoted are for an assumed thermospheric temperature of 700 K. We will make the approximation that $[e] \approx [O^+]$ and assume a Chapman layer for $[e]$ with a peak altitude of 300 km. In contrast to the calculations by Miller (1996), we found that we cannot ignore the terms in the denominator of (A.26). In addition, we will use more realistic profiles for the concentrations of N_2 and O_2 by using the MSIS-86 model. The result is

Table A.3 Constants for 630.0 Volume Rate Emission

Constant	Value	Reference
$A_{630.0}$	$5.63 \times 10^{-3}\,\text{s}^{-1}$	Sobral
$A_{636.4}$	$1.82 \times 10^{-3}\,\text{s}^{-1}$	Sobral
k_1	$1.06 \times 10^{-11}\,\text{s}^{-1}\,\text{cm}^3$	Sobral
k_2	$2.30 \times 10^{-11}\,\text{s}^{-1}\,\text{cm}^3$	Sobral
k_3	$3.20 \times 10^{-11}\,\text{s}^{-1}\,\text{cm}^3$	Sobral
k_4	$6.60 \times 10^{-10}\,\text{s}^{-1}\,\text{cm}^3$	Sobral
β	1.1	Bates
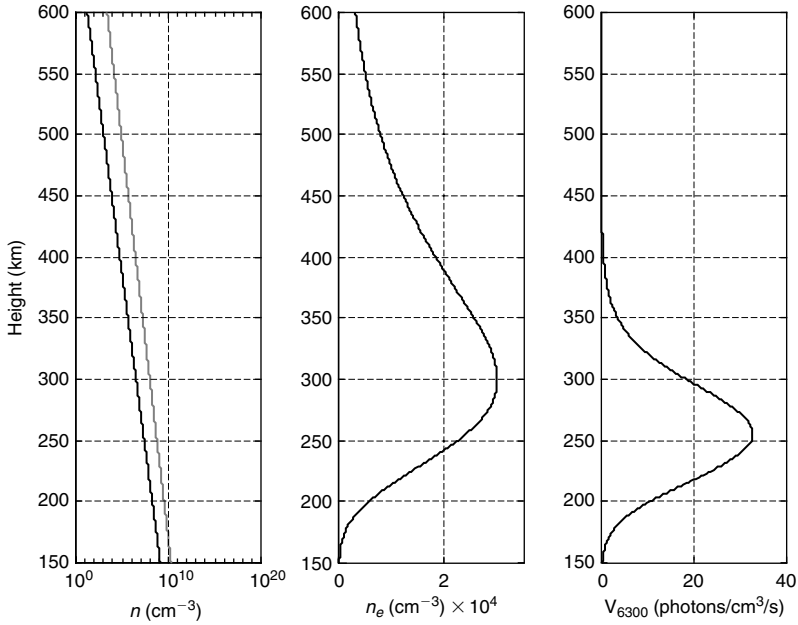
Figure A.11 630.0 nm airglow volume emission rate profile. The leftmost panel shows the assumed O_2 and N_2 densities (N_2 being the larger one) from the MSIS-86 model. The center panel gives the e^- profile a Chapman layer with a peak height of 300 km. The rightmost panel shows the corresponding volume emission rate profile.

shown in Fig. A.11. The total airglow intensity viewed from the ground is given by the height integral of the volume emission rate. It is clear that if the electron density profile were to rise the airglow intensity would fall because of the exponential drop-off of the O_2 concentration. For the same reason the intensity would increase if the electron density profile fell. Therefore, intensity variations in the 630.0 nm emission are in many instances associated with fluctuations in the height of the F peak. Note that the peak of the volume emission rate is approximately 50 km below the peak in electron density. It is also important to note that the half-width of this emission is almost an order of magnitude larger than those of the mesospheric emissions. The form of (A.26) is very similar to that for the Pedersen conductivity and can be used to determine that parameter (Makela and Kelley, 2003).

Oxygen Recombination Lines

The reaction

$$O^+ + e^- \rightarrow O + h\nu \tag{A.27}$$

is very slow because it is difficult to conserve energy momentum in this type of reaction. Several emissions can occur in this reaction, only one of which is detectable on the ground—that is, at 774 nm. The *TIMED* satellite uses the 139.4 nm emission, an example of which was presented in Fig. 6.15b. The equatorial arcs are plainly visible, as are striations due to depleted plasma wedges due to CIS/ESF. Figure 6.15b also shows a simultaneous 777.4 nm emission taken from Hawaii, which were used to identify the depleted light regions. For an O^+ plasma, the emission is proportional to $(n_e)^2$ and so is independent of height. A combination of 630 nm and 777.4 nm can thus be used to determine the height of the ionosphere (Makela et al., 2001).

A.2.2   Lidar

For a lidar, the scattering equation has the form,

$$E_r(\lambda, R) = E_t \xi(R) T(\lambda, R) \beta(\lambda) \xi(\lambda) \frac{A_0}{R^2} \Delta R$$

This version of the lidar equation corresponds to the case of Rayleigh backscatter.[2] E_t is the energy per pulse transmitted from the laser. The two-way attenuation coefficient is defined as $T(\lambda, R) = \exp[-\int \kappa(\lambda, R)dR]$, where $\kappa(\lambda, R) = \kappa(\lambda_t, R) + \kappa(\lambda_S, R)$ are inverse attenuation lengths for the transmitted and scattered radiation. The squiggles, ζ, represent system efficiency. The first squiggle is an overlap factor between the transmitter and receiver fields of view since these are often different in lidar systems. The second describes spectral losses in the receiver fields of view since these are often different in lidar systems. The second describes spectral losses in the receiver system—for example, due to narrow band optical filters and the quantum efficient of photo tube detectors. $\beta(\lambda) = \Sigma(\lambda)/V_s$, as defined in the previous section, is the volumetric backscatter cross section per unit solid angle [m^2/m^3]. With the lidar equation defined in terms of $\beta(\lambda)$, we have already circumvented the hard versus solid target discussion by assuming an extended scattering volume. The receiver acceptance solid angle is A_0/R^2, where A_0 is the physical area of the receiving telescope. It should be mentioned that lasers typically emit light which is much more directional than that of radar radiation patterns, so the approximation $\Omega \approx \lambda^2/A_{beam}$ is even better than for a radar system. The range resolution, ΔR, is again defined as $c\tau_r/2$, where τ_r is the sampling time. In lidar work the pulses (τ_t) are very short and each one is used to illuminate a ΔR much larger than the pulse length—that is, $\tau_t \ll \tau_r$.

In the laser community, it is typical to speak in terms of energy per pulse. However, an alternate form of the lidar equation is obtained by dividing by

---

[2] Taken from the Lidar School, CEDAR 1991, Eq. (7.14), in the book by Measures.

$\tau_t(\tau_r/\tau_t)$ [R. M. Measures, *Laser Remote Sensing: Fundamentals and Applications*. Krieger, Florida, 1992; Eq. (7.21)]

$$P_r(\lambda, R) = \left(\frac{\tau_t}{\tau_r}\right)P_t\xi(R)T(\lambda, R)\beta(\lambda)\xi(\lambda)\frac{A_0}{R^2}\Delta R \tag{A.28}$$

where the ratio (τ_r/τ_t) defines the equivalent number of laser pulses of length τ_t, which contributes to τ_r such that $(\tau_t/\tau_r)P_t$ is the average transmitted power in the sampling interval.

We can rewrite the physical area as an effective area to include the efficiency terms as $A_{eff} = \xi(\lambda)\xi(R)A_0$. For simplicity, we will assume that the transmissiveness is on the order of unity when working in the visible wavelength regime. With these changes the following form,

$$P_r = \left(\frac{\tau_t}{\tau_r}\right) P_t\beta\Delta R \frac{A_{eff}}{R^2}$$

which is nearly identical to the radar counterpart in Eq. (A.27).

Going a step further, it is interesting to note the similarity in the incoherent scatter (see Section A.1.1) and Rayleigh backscattering cross sections. We write the scattering cross section in the following suggestive form to highlight the similarity between the two methods:

$$\beta = N(Sr_e)^2; S = 1 \text{ Plasma}$$

$$\beta(\lambda) = N(Sr_e)^2 \left[\frac{500}{\lambda(nm)}\right]^4; S = 0.1 \text{ Rayleigh}$$

In these equations, N is the number density of scatterers and r_e is the classical electron radius.

The factor S has been included to take into account differences due to free versus bound electron scattering. As defined here, $S = 1$ for the case of a free electron plasma and $S = 0.1$ for atmospheric Rayleigh scattering at 500 nm wavelength. The results indicate that the cross section for unbound electrons (plasma) is roughly two orders of magnitude greater than that for bound electron states (typical of atmospheric constituents). Substituting these expressions for the cross section into our common form of the radar/lidar equation, we arrive at a final version of the two equations:

$$P_r = P_tN(Sr_e)^2\Delta R\frac{A_{eff}}{R^2} \quad \text{Radar} \tag{A.29}$$

$$P_r = \left(\frac{\tau_t}{\tau_r}\right) P_tN(Sr_e)^2\Delta R\frac{A_{eff}}{R^2}\left[\frac{500}{\lambda(nm)}\right]^4 \quad \text{Lidar} \tag{A.30}$$

Table A.4 Comparisons of Typical Parameters

	Radar	Lidar
P_t	10^6 Watts	10^8 Watts
N	$10^5 \, \mathrm{cm}^{-3}$	$10^{13} \, \mathrm{cm}^{-3}$
S^2	1	$(0.1)^2$
A_r	$7 \times 10^4 \, \mathrm{m}^2$	$0.4 \, \mathrm{m}^2$
τ_t/τ_r	1	1/1000
P_t	8.3×10^{-15} Watts	4.8×10^{-15} Watts

As a hypothetical application, neglecting efficiency terms, we compare the power returned from 100 km with 1.5 km range resolution for both the Arecibo radar (noontime) and lidar (night or day) as indicated in Table A.4.

The power received is of the same order of magnitude. However, experimental reality dictates that such measurements, while routine for the radar, are not possible for Rayleigh lidar. To see the difference, consider the results in terms of the number of photons received per pulse, obtained by dividing the power received by the energy per photon per range bin time (τ_r):

	Radar	Lidar
Photons/pulse	290,000	0.13

Though it is not typical to speak in terms of photon energy with the longer radar wavelengths, it is interesting to think in these terms. For the radar, the corresponding noise level is about 5000 photons per pulse so the S/N is high during the day. At night, the plasma density drops below $10^3 \, \mathrm{cm}^{-3}$ at 100 km and the radar signal-to-noise becomes of order unity. It is clear that, even at night, the lidar signal will be lost in a background noise at this altitude. However, as the sampling altitude decreases below 100 km, lidar systems consistently improve, while the radar S/N remains small. The next step involves studying the complex factors that determine the system noise, a step that is beyond the scope of this book.

A Rayleigh lidar scatters from molecules in the atmosphere. The cross section thus decreases exponentially with altitude. Resonance lidars use resonant (fluorescence) scattering from metallic atoms that have a cross section many orders of magnitude larger than the atmosphere at typical heights where the atoms are found. Using such scatterers extends the useful height of the lidar method.

Figure A.12 shows a profile of photon counts versus altitude for a sodium lidar. Rayleigh, aerosol, resonant, and meteor trail scatter can be seen in the plot. Boltzmann lidars use the ratio of atoms in different atomic states to determine temperature. Lidars having very narrow line widths can be used to measure winds that cause a measurable Doppler shift.

Figure A.12 showing photon count as a function of altitude.
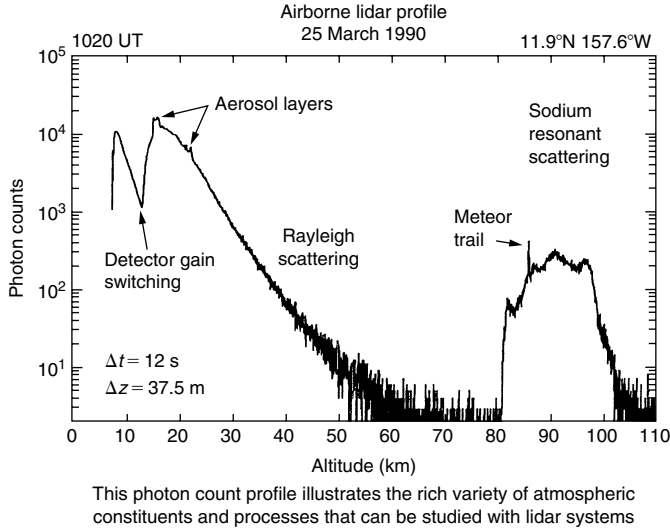
Figure A.12 Photon count as a function of altitude for a sodium lidar. (Figure courtesy of Chester Gardner.)

Fabry-Pérot Interferometery Thermospheric/Ionospheric Measurements

At the heart of a Fabry-Pérot interferometer (FPI), a two parallel, flat, semi-transparent mirrors separated by a known distance (i.e., an etalon), invented in the late 1890s by Charles Fabry and Alfred Pérot. The usefulness of the instrument is made apparent when one understands that the FPI is the most luminous instrument for a given resolving power. As such, the FPI has made its appearance in a large number of disciplines, from basic spectroscopy, to laser cavity development, to optical computing, to the telecommunications industry. An excellent review of the FPI is given by Hernandez (1986) and is considered to be a "classic text" on the instrument. A system schematic is presented in Fig. A.13.

The first application of the FPI to thermospheric/ionospheric measurements was by Babcock (1923) with measurements of the upper mesospheric green line at 557.7345 nm, now known to be the $O(^1S) \rightarrow O(^1D)$ transition of atomic oxygen (OI). This particular line is generated in a narrow altitude region centered around $\sim$96 km altitude, and spectroscopic measurements of the emission line result in a measured Doppler shift and Doppler broadening when compared to a reference line. The Doppler shift can be converted to absolute wind measurements via

$$\frac{v_r}{c} = \frac{\lambda_m - \lambda_o}{\lambda_o} \tag{A.31}$$

where v_r is the radial component of the wind velocity (and thus requires multiple measurements to obtain the full wind vector), λ_m is the measured wavelength at
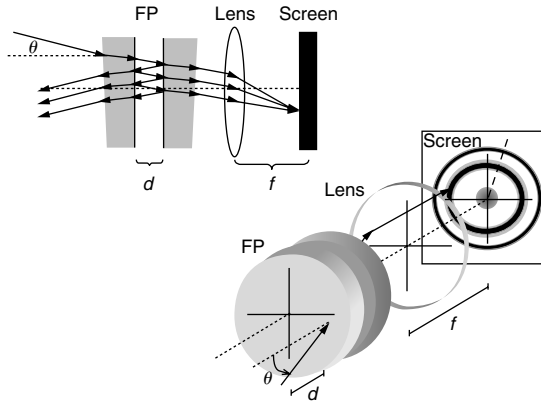
Figure A.13   Schematic of a Fabry-Pérot Interferometer. The screen can be considered a CCD detector. (Figure courtesy of Andrew Gerrard.)

the peak of the emission line, λ_m is the corresponding Doppler reference wavelength, and c is the speed of light. Temperature measurements use the Doppler broadening via the expression

$$T = \frac{m \cdot c^2}{2 \cdot k_B} \left(\frac{\Delta \lambda_m}{\lambda_m} \right)^2 - T_{instr} \tag{A.32}$$

where $\Delta \lambda_m$ is the measured $1/e$ half-width of the (assumed) Gaussian emission profile, T_{instr} is the equivalent instrument temperature due to the FPI instrument function (i.e., the spectral response of the FPI to a monochromatic source), k_B is Boltzmann's constant, and m is the mass of the constituent (other variables defined above). The FPI is the only remote sensing technique available for probing the upper atmosphere.

FPI observations of other atmospheric lines originating from different altitudes (e.g., those listed in Table A.5) can therefore yield important base-state dynamical parameters necessary for understanding the upper atmosphere. An excellent review of remote sensing of the middle and upper atmosphere via passive optical instrumentation and the science obtained from such data can be found in Meriwether et al. (2004). An example of nighttime wind and temperature measurements along with error bars is presented in Fig. A.14.

Particulars of the FPI

Discussions of how an FPI works can be found in numerous texts, from the undergraduate (e.g., Hecht, 1998; Klein and Furtak, 1986) to the graduate (e.g., Born and Wolf, 1999; Saleh and Teich, 1991) to the professional levels (e.g., a series of HRDI optical engineering papers by P. Hays and W. Skinner; see

Table A.5 Commonly Observed Upper Atmospheric Emission Lines in Angstroms

Vacuum Wavelength (Å)	Wavelength in Air* (Å)	Emitter	Science Applications
5578.887	5577.339	OI	Nighttime mesospheric winds and temperatures
6302.046	6300.304	OI	Nighttime and Daytime thermospheric winds and temperatures
7322.01	7319.99	O^+	Nighttime and Daytime thermospheric ion drifts and temperatures
8401.429/8401.527	8399.121/8399.219	OH	Nighttime mesospheric winds and temperature
8467.534/8467.835	8465.208/8465.509	OH	Daytime mesospheric temperatures from analysis of intensity ratios with 8400 Å

*Air is defined here as 15°C and 101,325 Pa, with 0.033% CO_2.
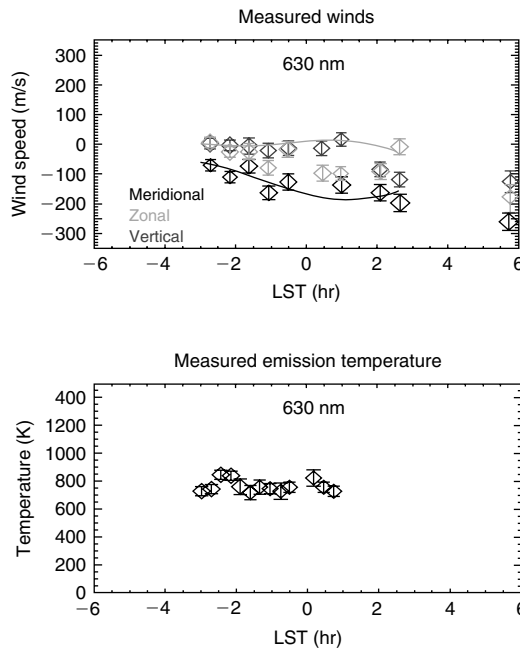
Figure A.14 Typical nighttime wind and temperature data obtained from 630 nm OI emission observed with the SOFDI instrument (described in the next section) located in Oneida, NY, over the night of September 9–10, 2005. Local Solar Time (LST) is denoted with 0 representing local midnight. Thin lines represent climatological winds. (Figure courtesy of Andrew Gerrard.)

Skinner et al., 1987). The analyses focuses on the optical arrangement depicted in Fig. A.1, where a Fabry-Pérot etalon (denoted FP) of gap distance, d, is placed in front of a lens of focal length, f. Because of the multiple reflections occurring within the etalon, multiple "images" of the source are formed that differ by a set phase difference. This is similar to the multiple images formed by double-paned glass windows. These images are combined by use of the focusing lens which forces the multiple rays to interfere at some spot on the screen. Hence, the interference takes place because of the lens, not the etalon (whose role is to create the multiple images, each with a set phase difference).

A typical pattern created by a diffuse source is depicted on the screen in Fig. A.13. A radial slice of this bull's-eye pattern would yield a cross section similar to that in Fig. A.15. This latter figure illustrates the nature of the FPI fringe pattern under different conditions. We note that this cross section is in "pixel space" (i.e., the x-axis is represented in CCD pixels) and would need to be converted to "wavelength space" before Eqs. (A.31) and (A.32) are utilized.

An Example of a Contemporary FPI

In this final section we present a contemporary FPI, the Second-generation, Optimized, Fabry-Pérot Doppler Imager (SOFDI). At its core, SOFDI is a triple etalon
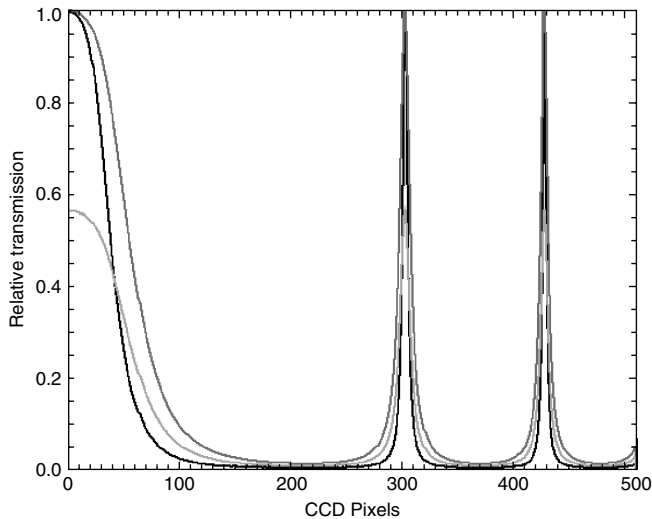
Figure A.15   Idealized FPI instrument functions for a monochromatic 630 nm line with a $\sim$2.3 mm etalon gap (d) and 23.7 cm focal length (f) for various reflection (R) and absorption (A) terms. No plate defects parameters are included. x-Axis is in CCD pixels, measured from the center of the screen outward. Black Line: $R = 90\%$, $A = 0$. Red Line: $R = 80\%$, $A = 0$. Green Line: $R = 80\%$, $A = 5\%$. Plate defect terms tend to further lower transmission and broaden the fringes. (Figure courtesy of Andrew Gerrard.)

Fabry-Pérot interferometer capable of making wind and temperature measurements from the spectra obtained from various middle and upper atmospheric emission lines. Table A.5 gives a list of the various emission lines measurable by SOFDI.

The extension of a traditionally nighttime technique/measurement into the daytime regime comes with a considerable increase in instrumental complexity in SOFDI. Specifically, additional etalons, serving to both decrease the transmission width of the overall instrument function/response and to block adjacent transmission windows which are located at integer values of the free spectral range from the primary order of interest, need to be included into the optical system. The end effect is to approximate a delta function instrument response which is centered on the emission line of interest (i.e., herein, we use the term *signal* to represent the light collected from the desired emission). These additional etalons ultimately reduce the solar "noise" continuum, thus increasing the signal-to-noise ratio of the measurement.

The SOFDI FPI instrument is housed within a relocatable trailer, sized to fit inside a standard shipping container and equipped with a combined light/sound alarm system. The trailer requires an electrical hookup providing 10 kW peak power, with which internal transformers condition input power as needed and offer protection against electrical surge, brownouts, and so forth, and a network connection, with which the entire SOFDI instrument can be started, operated, rebooted, and shut down remotely. These two relatively available commodities make operation of the trailer in remote locales much less costly, especially in regard to personnel costs [e.g., in 2009 SOFDI is scheduled to travel to Huancayo, Peru, to undertake remote operations under the magnetic equator in collaboration with the Air Force Communications/Navigation Outage Forecasting System (C/NOFS) satellite]. Heating and air conditioning units keep the internal trailer temperature at $26.5°C \pm 0.5°C$.

A.3   In Situ Measurements

Satellite and rocket-borne instrumentation of all kinds has greatly added to our knowledge of the ionosphere. Here we concentrate on techniques that are used to determine ionospheric parameters such as density, temperature, drift velocity, and electric fields. The treatment is not exhaustive but is representative of some of the instrumentation referred to in the text. Other reviews of interest are by Bauer and Nagy (1975) and Mozer (1973).

A.3.1   Langmuir Probes, Retarding Potential Analyses, and Drift Meters

In this section we deal with a variety of instruments used to measure the temperature, concentration, and drift velocity of either the ambient thermal electrons

or the thermal ions. These instruments are mounted on satellites and rockets that are moving through the plasma at velocities between 1 and 9 km/s. In such cases any conducting surface will collect an electron current and an ion current that can be calculated by assuming that the plasma has a drifting Maxwellian distribution function. If the conductor is held at some potential P, the current is calculated by integrating the distribution function over the surface area of the collector for all energies greater than P.

In the earth's ionosphere, the bulk velocity of the electrons with respect to a satellite or rocket is much smaller than the thermal velocity of the electrons. Electron current is therefore collected by all exposed conducting surfaces at a potential that will allow it. The bulk velocity of the ions with respect to a satellite or rocket is, however, comparable to or greater than their thermal velocity. Thus, the ion current to a probe can depend on the orientation of the collecting surface with respect to the relative velocity vector. If the spacecraft were maintained at zero potential with respect to the plasma, then it can be seen that it would collect more electron current due to the higher mobility and larger available collection area than the ion current. The spacecraft does not, however, draw a current from the plasma, and therefore the spacecraft will assume a negative potential with respect to the plasma such that the net current is zero. The spacecraft potential, which is also the ground potential of any probe connected to it, causes a region of positive charge to build up around it from which the electrons are repelled. This region is known as the sheath.

Electron Temperature Measurements—The Langmuir Probe

Mott-Smith and Langmuir (1926) published a classical paper on the current collection properties of a probe in a plasma from which the modern Langmuir probe derives its name. Most Langmuir probes consist of small conducting surfaces with cylindrical or spherical geometries. Typical sensor dimensions are a 2-centimeter-diameter sphere or a 20-centimeter-long, 0.2-centimeter-diameter cylinder. The probes are usually mounted on short booms of about 20 cm length to project beyond the spacecraft sheath. As mentioned before, the current collection properties of these probes depend on the shape and area of the collector. As we shall see, however, they do not have a large effect on the determination of electron temperature. The instruments function by applying a varying voltage to the probe that covers the range of energies of interest. Typical probe voltages may vary between $+5$ and -5 V. Figure A.16 shows a characteristic curve of probe current versus voltage that one might obtain from a cylindrical Langmuir probe. In fact, all Langmuir characteristic curves have the same regions. The ion saturation region occurs where the probe potential is sufficiently negative to repel all the thermal electrons and begin to attract the ions. The electron retardation region exists where the ion current is not affected greatly by the potential on the probe, but some electrons are repelled. Finally, the electron saturation region exists where all the thermal electrons are attracted to the probe and where the
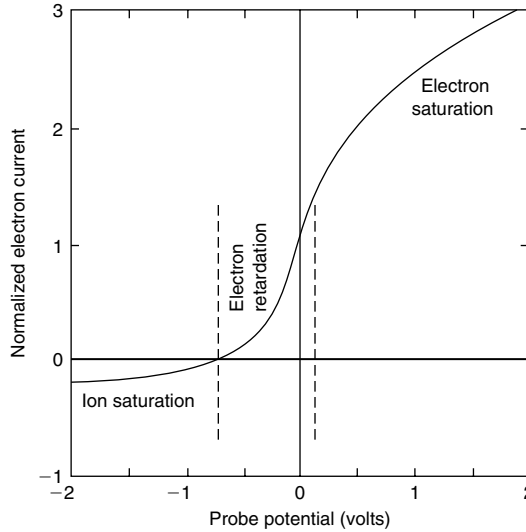
Figure A.16 A typical Langmuir probe I-V characteristic.

probe potential repels the ion current. In the electron retardation region the probe current is given by

$$I_e = N_e q A \left(k_B T_e / 2\pi m_e \right)^{1/2} \exp(-q\Phi/k_B T_e)$$

where A is the collector area, N_e the electron concentration, q the electron charge, k_B the Boltzmann constant, T_e the electron temperature, m_e the electron mass, and Φ the retarding potential applied to the probe.

A variety of techniques can be employed to extract the electron temperature from such a characteristic curve. If a least-squares fit to the original data can be performed, then either knowledge of the electron concentration is required or this parameter must also be a least-squares variable. An alternative lies in considering the logarithm of the electron current rather than the current itself. Taking the logarithm of both sides of the previous equation,

$$\ln(I_e) = -q\Phi/k_B T_e + \ln(\text{const})$$

Thus, the logarithm of the output from this device in the electron retardation region should be a straight line for which the slope is proportional to the electron temperature. Using this result, it is possible to use on-board microprocessors to derive the electron temperature directly.

In the two saturation regions, the ion current and the electron current can be obtained by integrating the appropriate drifting Maxwellian energy distribution function over the collector surface for all energies less than the probe potential.

These currents depend on the sensor geometry and, as can be seen in Fig. A.19, they need not saturate at potentials less than 5 V. We will deal with the ion saturation of a planar probe in the discussion of retarding potential analyzers. In the so-called electron saturation region the electron current to a cylindrical collector is given approximately by

$$I_e = 2AN_e q \left(\frac{k_B T_e}{2\pi m_e}\right)^{1/2} \frac{1}{\pi^{1/2}} \left(1 + \frac{q\Phi}{k_B T_e}\right)^{1/2}$$

This expression is derived from the assumption of an infinitely long cylinder and therefore has an "end effect" correction that is usually small for typical cylindrical probe dimensions (Szuszczewicz and Takacs, 1979). Having derived the electron temperature from the electron retardation region, it can be seen that the electron saturation portion of the curve can be simply used to derive the electron concentration. In fact, the ion saturation portion of the curve can be similarly used to calculate the total ion concentration. The latter has the advantage that when the probe velocity is much greater than the thermal velocity of the ions, the expression for the total ion concentration is essentially independent of the ion temperature and a very small end effect correction. Since the ionospheric plasma is charge neutral, this approach is frequently employed to derive the total plasma concentration from a Langmuir probe.

Ion Temperature and Density Measurements—The Retarding Potential Analyzer

Retarding potential analyzers (RPAs)[3] measure the ambient ion current to a collector as a function of an applied retarding potential. In a manner similar to a Langmuir probe, a curve of ion current versus retarding potential is obtained from which the thermal ion temperature can be determined.

The velocity of an earth-orbiting satellite can be as high as 8 km/s in the ionosphere. At this velocity the kinetic energy of the ions ($1/2\ m_i V^2$) is equivalent to 1/3 eV/amu. The presence of molecular and metallic ions (Fe^+) in the ionosphere therefore requires that retarding potentials between 20 and 30 V be applied in the sensor. An RPA sensor typically has a planar or spherical geometry. A spherical geometry has the advantage that it can be mounted on a spacecraft in such a way that it has access to the flowing ion gas for most orientations of the spacecraft. The plasma sensor must, however, be mounted to view along the velocity vector of the satellite, thus precluding measurements more than once per spin period if the vehicle is spinning. The planar sensor has the advantage that its known orientation with respect to the spacecraft velocity allows additional information to be extracted from the curve of ion current versus retarding potential. In addition,

---
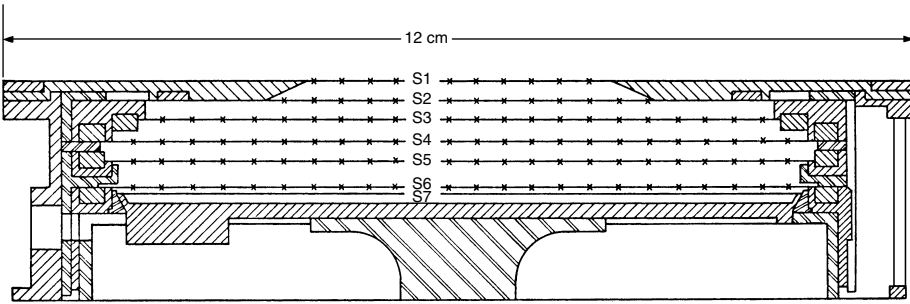
[3] Figures courtesy of R. Heelis.

Figure A.17   Grid arrangement for a plasma retarding potential analyzer.

the construction of a planar geometry leads to more uniform electric potentials in the sensor.

The sensor consists of a collector to which the current-measuring electronics is attached and which is usually grounded to the spacecraft. Placed between the collector and incoming plasma stream is a series of grids. We will describe the operation of a planar sensor as shown schematically in cross section in Fig. A.17. In this configuration the collector S7 is grounded through the current-measuring electronics and the grid S6 is grounded to ensure that no induced currents are seen by the collector. The grid S5 is biased negatively (typically -25 V) to prevent ambient electrons from reaching the collector and to suppress any electrons liberated from the collector by solar ultraviolet radiation. The grids S4 and S3 have the retarding potential applied to them. This potential may take a variety of waveforms in the range 0 to $+30$ V. Finally, the entrance grids S2 and S1 are grounded to the external plane of the instrument to ensure that an electrically uniform, uncontaminated environment is presented to the plasma.

The ion current at a given retarding potential depends on the ion flux reaching the collector for all ion species with energy greater than the applied potential. This quantity can be obtained by integrating the ion velocity distribution function over the collector surface. The simplest expression is obtained for a planar surface and is given by

$$I = \frac{1}{2}\alpha V A_q \Sigma_i N_i \left[1 + erf(\beta_i f_i) + \frac{1}{\pi^{1/2}\beta_i V} \exp\left(\beta_i^2 f_i^2\right) \right] (\hat{n} \cdot \mathbf{v})$$

where

I = collector current	$\hat{n}$ = unit vector normal to sensor face
α = grid transmission factor	$\mathbf{v} = \mathbf{v}_d - \mathbf{v}_p$
A = aperture area	$\mathbf{v}_p$ = sensor velocity
N_i = concentration of ith ion	$\mathbf{v}_d$ = ambient ion drift velocity
$V = \mathbf{v} \cdot \hat{n}$	$f_i = V - [2q(\Phi + \Phi_0)/m_i]^{1/2}$

$$\beta_i = \left(m_i/2k_B T_i\right)^{1/2} \qquad k_B = \text{Boltzmann's constant}$$
$$m_i = \text{mass of } i\text{th ion} \qquad \Phi = \text{retarding grid potential}$$
$$T_i = \text{ion temperature} \qquad \Phi_0 = \text{spacecraft potential}$$

Figure A.18 shows some representative curves of the ion current versus retarding potential that would result from such a sensor operated on an earth-orbiting satellite. The light ions H^+ and He^+ have very little ram energy and thus appear at low retarding voltages. Successively heavier masses appear at higher retarding potentials due to their higher ram energy. The effect of larger ion temperatures is also apparent when comparing frames d and e of Fig. A.18. Higher temperature also supplies the ions with higher energies, and thus the curve appears "fatter" than a curve with lower ion temperature. Given the number of mass species and the mass numbers, a nonlinear least-squares fitting of the data to the preceding expression will yield a common ion temperature, the constituent ion concentrations, and the bulk ambient ion drift velocity.
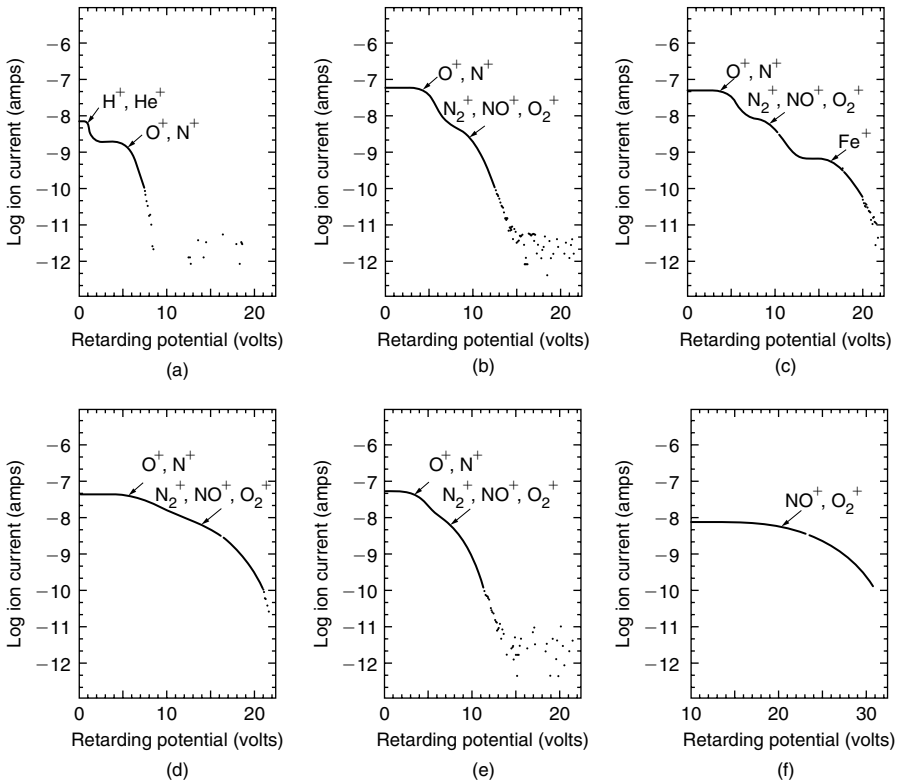

Figure A.18   Sample RPA curves for various ionospheric conditions.

Ion Drift Velocity Measurements—The Ion Drift Meter

We have seen that a planar RPA is capable of measuring the component of the ion drift velocity along the look direction of the sensor. In the earth's ionosphere, where an orbiting spacecraft moves at a velocity much larger than the ion thermal speed, a rather simple device called an ion drift meter (IDM) can be used to measure the other two mutually perpendicular ion drift velocity components. The IDM has a planar geometry similar to the RPA but has a square entrance aperture and a segmented collector as shown schematically in Fig. A.19.

The grid S5 is biased negatively to prevent ambient electrons from reaching the collector and to suppress any photoelectrons liberated from the collector surface. All other grids are grounded to ensure a field-free region between S2 and S3 through which the ambient ions can drift. Since the ions are moving supersonically with respect to the sensor, they form a collimated beam in the manner shown in Fig. A.20. The collector area which they illuminate will therefore depend on the angle at which they arrive at the sensor. Since the current collected on each collector segment is proportional to the area struck by the ion beam, it can be shown quite easily that the ratio of the currents of two segments is proportional to the tangent of the ion arrival angle. If the entrance aperture has straight edges and the currents to each collector pair are denoted by I_1 and I_2, then

$$\log I_1 - \log I_2 = \log(I_1/I_2) = \log\left[(H + D\tan\alpha)/(H - D\tan\alpha)\right]$$

If we let $I_1 - I_2 = \Delta I$ and let $I = I_1 + I_2$, then to first order in $\Delta I/I$ we can show that

$$\log I_1 - \log I_2 = (2H/D)\tan\alpha$$

Thus, by using a combination of logarithmic amplifiers to measure the collector current and a linear difference amplifier to supply the difference in the signals, it is possible to obtain the ion arrival angle directly. A similar geometry in the
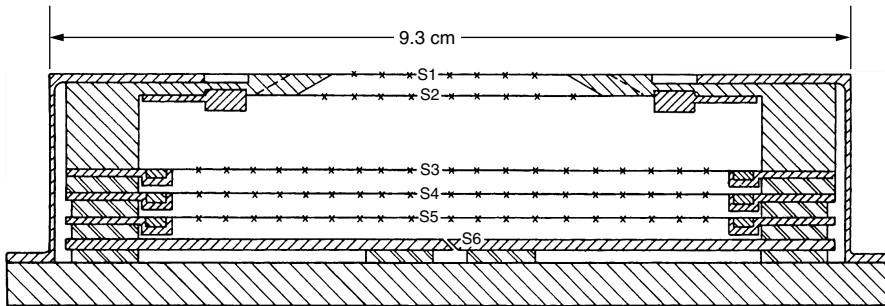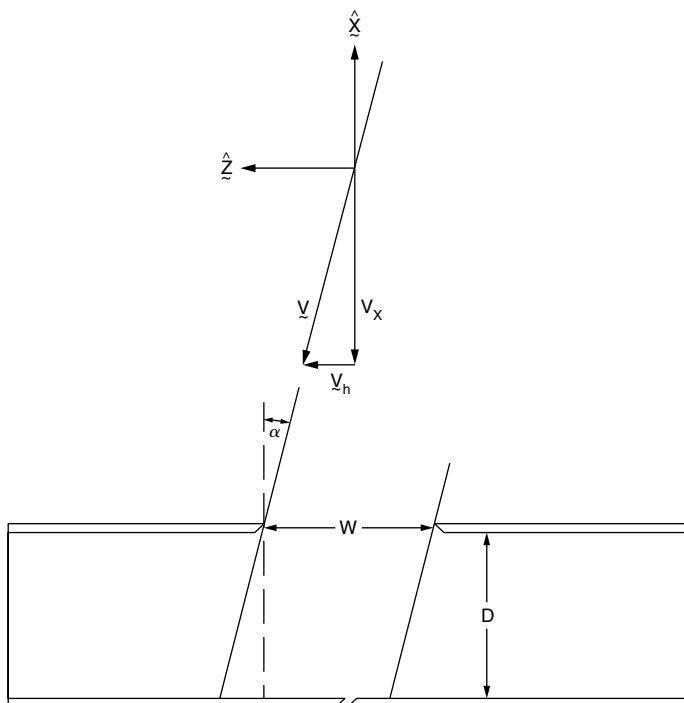

Figure A.19   Modification of a plasma ion sensor to measure the plasma drift velocity.

Figure A.20   Illustration of the geometry involved in the interpretation of measured particle arrival angles.

plane perpendicular to the paper can be obtained by considering two appropriate pairs from quadrant segments of the collector. Thus, two mutually perpendicular ion arrival angles can be obtained from a single sensor. These arrival angles can easily be converted to velocities relative to the spacecraft from knowledge of the ram drift obtained from the RPA. Without this information usually only a small error is introduced by using the spacecraft velocity along the look direction. To convert all these velocities into ambient ion drifts it is necessary to subtract the components of the spacecraft velocity from each direction. This requires knowledge of the orientation (attitude) in inertial space, which is usually obtained from a combination of star sensors, sun sensors, and horizon sensors.

Ion Composition Measurements—The Mass Spectrometer

The thermal ion devices we have described so far require the detection of the current produced by an ion striking a conducting surface. These devices are therefore incapable of detecting ions if the conducting surface is too small or the number of ions striking the conductor is too small. The RPA we have described distinguishes only a lower limit to the energy of the ions striking the collector

and it therefore cannot easily distinguish a small number of ions with small mass immersed in a larger number of ions of larger mass. This is frequently the situation between, say, 500 and 1000 km, where the O^+ concentration exceeds the H^+ and He^+ concentrations. Mass spectrometers are utilized for the detection of very low concentrations of constituent species.

Most mass spectrometers employ high-sensitivity detectors for measuring the constituent ion concentrations. These detectors are called electron multipliers, and they detect the presence of a single charged particle by a cascade of electrons that is produced when it strikes the surface of the multiplier. Preceding the detector is an analyzer that selects the mass of the particle to be detected. Many different techniques are employed in distinguishing ions of different masses, but in common use for ionospheric studies are three basic types: the magnetic analyzer, the radio frequency analyzer, and the quadrupole analyzer. The magnetic and drift analyzers use a preacceleration potential P that is much larger than the thermal energy of the ions being detected. Thus, all ions enter the analyzer with a discrete velocity V given by

$$V^2 = 2Z\Phi/M$$

where M is the ion mass and Z denotes the charge state of the ion.

In a magnetic analyzer the application of a uniform magnetic field B perpendicular to the initial velocity vector will cause the ion to begin a gyromotion. Application of the simple equations of motion for a charged particle in a magnetic field will show that the radius of curvature of this motion is given by

$$R = (1/B)(2MV/Z)^{1/2}$$

Thus, ions of larger mass will have a larger radius of curvature than ions of smaller mass. Alternatively, one may arrange for ions of different masses to describe the same radius of curvature in the magnetic field by adjusting their entrance velocity, that is, by adjusting the potential Φ. Figure A.21 shows schematically the trajectories of ions in a 180° magnetic sector. At the image plane it is possible to use a single detector and scan the potential Φ to observe all masses. Alternatively, multiple-detector arrays, known as microchannel plates, can be used to detect simultaneously a portion of the mass spectrum that is directed to the image plane. Finally, we should note that an ambiguity can exist in distinguishing between mass number and charge state. For example, doubly charged helium ions of mass 4 and deuterium ions of mass 2 will appear at the same location for a given potential Φ. It is necessary to resolve the momentum differences between such ions in order to separate them in a magnetic analyzer. Magnetic spectrometers in use today have a variety of sector lengths from about 60° to 180°.

The radio frequency mass spectrometer was introduced by Bennett and is sometimes called a Bennett tube. It functions somewhat like a linear accelerator
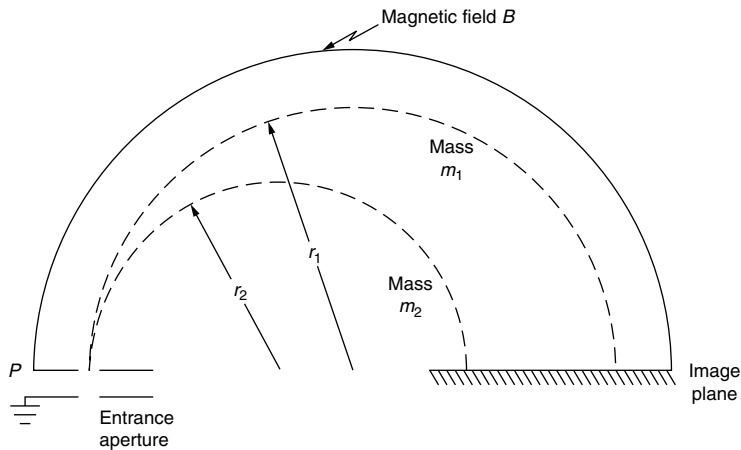
Figure A.21 The trajectories of ions with different masses in a magnetic field may be used to distinguish them.
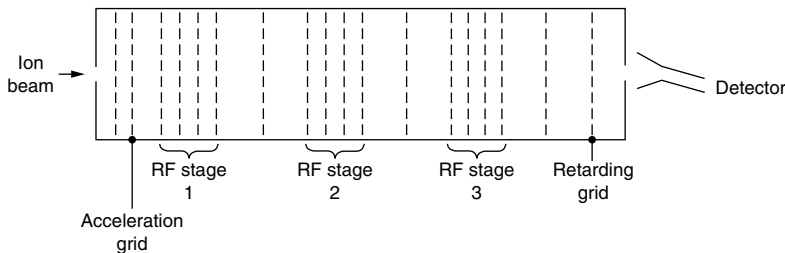
Figure A.22 Illustration of the rf stages in a Bennett tube.

and is shown schematically in Fig. A.22. The spectrometer has several "stages" consisting of groups of rf modulating grids. The ions are injected into the instrument so that they all have approximately the same energy, as in the case of a magnetic spectrometer. The rf grid system then selectively accelerates and decelerates ions of different mass because they will have entered the instrument with different velocities. The incremental velocity added or subtracted from an ion will depend on the phase of the grid cycle, and maximum velocity addition will occur for unique values of the ion velocity (i.e., ion mass) and phase angle. At the exit of the detector a retarding grid is used to select only those ions receiving the maximum acceleration. Electron multiplier detectors are again utilized and mass scanning is achieved by appropriately adjusting the analyzer draw-in potential, the frequency of the rf oscillator, and the bias of the retarding grid.

In addition to the magnetic and rf spectrometers, the quadrupole spectrometer is in common use for detecting neutral and ion species in the ionosphere. This spectrometer is so called because it consists of four hyperbolically shaped
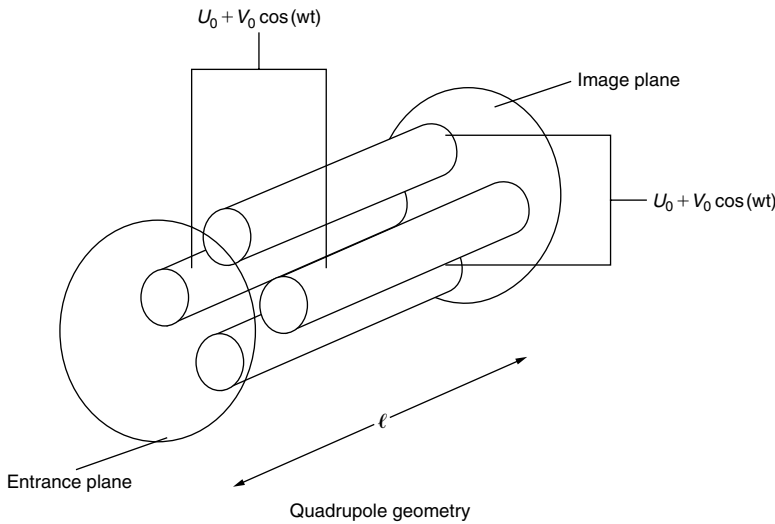
Figure A.23   Geometry of a quadrupole ion mass spectrometer.

electrodes of length *l* to which a combination of dc and radio frequency voltages is applied. This is shown schematically in Fig. A.23. The basic concept is to provide a potential field within the instrument which is periodic in time and symmetrical about the transmission axis. The frequency of the periodic potential is such that the transmission time along the axis length is long compared to the rf period. This spectrometer has the property that the draw-in potential is much less than that used in the magnetic or Bennett spectrometer, so the thermal motion of the ions is important. By adjusting the applied potentials it is possible to allow an ion of a particular mass-to-charge ratio to pass through the system and to ensure that all other ions undergo oscillating trajectories of increasing amplitude so that they are trapped on one of the electrodes before moving the distance 1. Again, electron multiplier detectors are used at the instrument exit to achieve extremely high sensitivities. This device and the Bennett tube are not amenable to the use of microchannel plates but are frequently used when concerns about weight preclude the use of a magnetic analyzer or when neutral mass spectrometry not requiring high time resolution is performed.

A.3.2   Electric Current, Measurements—The Fluxgate Magnetometer

The presence of electric currents, both on the ground and in space, is detected by the variations from the background magnetic field that they produce. A multitude of such measurements made by instruments in low earth orbit has allowed us to specify the earth's field with great accuracy. Spherical harmonic expansions are generally used with coefficients that are periodically updated to reflect

variations in the main field. If we let ΔB be a measured vector difference between the measured magnetic field and that calculated from a model, then Maxwell's equations allow us to specify this magnetic perturbation in terms of a current J by the expression

$$curl(\Delta B) = \mu_0 J$$

Devices for measuring these magnetic perturbation vectors are called magnetometers. Various techniques are employed in these instruments, but the most commonly used both on the ground and in space is a fluxgate magnetometer. This device behaves like a transformer with a core material that is magnetically saturable. Figure A.24 shows the operating principle of such a device. The input signal to the primary winding is a sinusoidal waveform of amplitude H_0 and period T. This is approximated by a triangular waveform in the figure. The amplitude of this primary signal is much larger than the ambient magnetic field
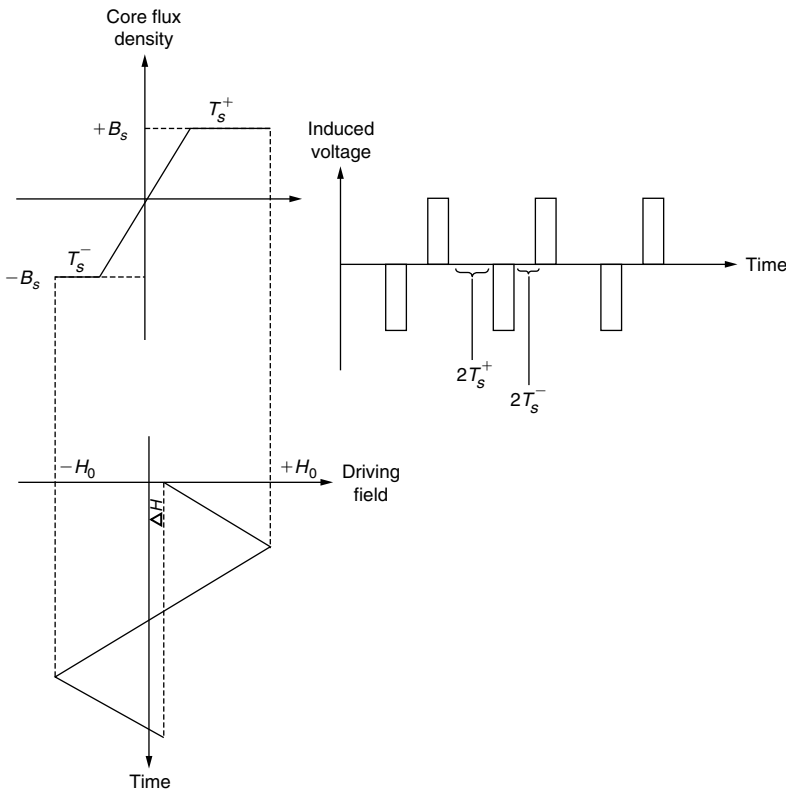

Figure A.24   Relationship between the external magnetic field and the induced voltage at the output of a fluxgate magnetometer.

component ΔH along the core. The ambient field therefore produces a small offset in the drive field. This small offset will cause the core flux to spend more time in one saturated state than in the other. In the case illustrated the time of positive saturation T_s^+ is greater than the time of negative saturation T_s^-. A voltage is induced on the secondary winding of the core only when the core flux density is changing. Thus, the output voltage will consist of a series of pulses that are unevenly spaced due to the different times spent in the saturated state. This is illustrated by the plot of induced voltage versus time shown in Fig. A.24. A Fourier analysis of the output signal shows that second harmonics of the primary driving frequency are present, only if the ambient field ΔH is nonzero. Further, the amplitude of the second harmonic is directly proportional to the sign and magnitude of $\Delta H/H_0$. In practice, the secondary harmonic output is obtained by appropriate electronic filtering of the output voltage. The so-called secondary harmonic type of fluxgate magnetometer has found the most extensive use in ground-based and spaceflight applications. It is important to note that J is not directly measured by such a system and that $\nabla \times \mathbf{B}$ is impossible to determine from a single spacecraft.

Other Current Measurement Technology

Attempts to measure all the charged particle fluxes and thus deduce the current have proved to be very difficult. In some auroral zone experiments a considerable fraction of intense upward currents has been accounted for by detection of the precipitating electron flux between, say, 10 eV and 20 keV. However, one is never quite sure how much current is carried by the lowest-energy electrons or thermal ions.

Faraday ring devices have been attempted to measure current directly (Torbert, personal communication, 1988). A laser is used to illuminate a loop of fiber optic cable. The change in polarization which results is a direct measure of the current threading the coil. The effect is small and technical problems abound but the reward would be well worth it if the development could be made.

A.3.3   Double-Probe Electric Field Detectors

The double-probe technique has been used successfully to measure electric fields on balloons, rockets, and satellites. In essence, at dc the technique makes a resistive contact to the plasma at two separated positions. If the two electrodes and their local interactions with the medium are sufficiently similar, then the difference of potential between the two electrodes equals the difference of potential between the two points in space. Dividing by the magnitude of the vector distance $\mathbf{d}$ between them yields the component of the electric field linking the two sensors.

The most symmetrical element is a sphere and many in situ electric field measurements use spherical electrodes mounted on insulating booms which are made as long as financial and mechanical constraints allow. The length is maximized since the voltage signal V_s is proportional to $V_s = -\mathbf{E}' \cdot \mathbf{d}$, whereas the sources

of error are either independent of the separation from the spacecraft or decrease drastically with separation distance. Typical boom lengths on sounding rockets range from 1 to 15 m, and on satellites 100 m tip-to-tip separations are commonly used.

Some of these error sources can be understood from the interaction between a single electrode and the local plasma. Consider first a floating probe, that is, one from which no current is drawn by the attached electronics. Due to their higher velocity, the flux of electrons to a given surface, nv_e, exceeds the flux of ions to the same surface, nv_i. An electrode will thus charge up negatively, repelling just enough electrons that the electron and ion fluxes are equal. For a spherical probe at rest with area A in a plasma of temperature T, with electron and ion masses m and M, the current I to the probe is given by

$$I = (Ane/4)(8k_BT/\pi M)^{1/2} - (Ane/4)(8k_BT/\pi m)^{1/2} \exp(eV_F/k_BT)$$
(A.33)

(Fahleson, 1967). Setting $I = 0$ for a floating probe and solving (A.8) for V_F yields

$$V_F = (k_BT/e) \ln(m/M)^{1/2}$$

For a 1000 K, O^+ plasma, $V_F = -5.1 k_BT/e \approx -0.44$ volts. Any asymmetries between the probes will make V_F differ and create an error signal. Sources of errors include asymmetric ion collection due to the spacecraft motion, which is usually at a velocity higher than the ion thermal speed, asymmetric photoemission, which behaves like an ion current to each probe, and asymmetric electron collection. The latter may arise if the main spacecraft emits photoelectrons that are collected by probes or if the magnetic field lines that thread one of the probes pass near the main spacecraft. An additional error signal comes from any possible difference in the average work function of the two surfaces.

The schematic diagram (Mozer, 1973) given in Fig. A.25 shows the potentials involved when two separated electrodes, with different work functions WF_1 and WF_2, different floating potentials V_1 and V_2, and separated by a distance **d** in an external electric field $\mathbf{E}'$ are connected to a differential electrometer with input resistance R. To make the measurement, a current I must be drawn by the electronics. This creates an additional potential difference at the two spheres denoted by $R_1 I$ and $R_2 I$, where

$$R_j = (\partial V/\partial I)_{V_F}$$

is the dynamic resistance of the electrode-plasma contact evaluated at the floating potential. Differentiating Eq. (A.33) and evaluating R at the floating potential yields

$$R = (k_BT/e)/I_i$$
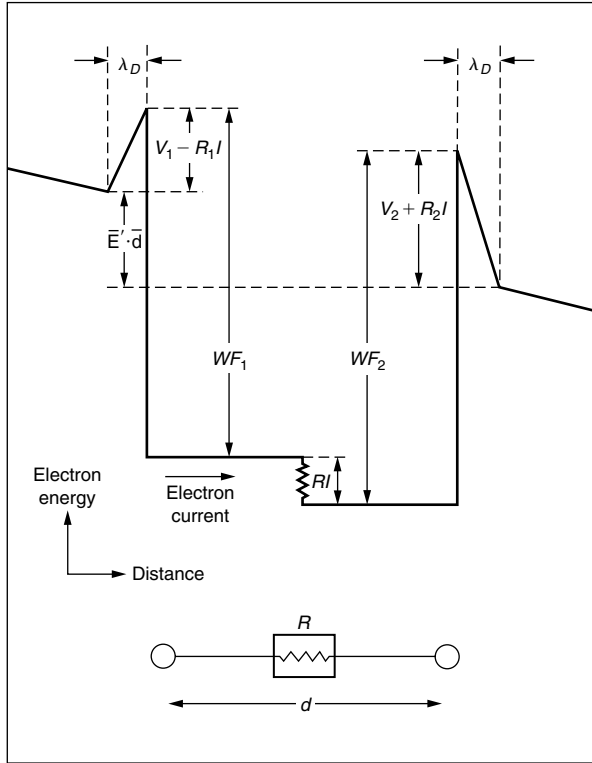
Figure A.25   Electron potential energy as a function of position near a Langmuir double probe. (Figure courtesy of F. Mozer.)

That is, the electron temperature measured in electron volts divided by the ion current to the probe yields the dynamic resistance for a floating probe. For a sphere of $100\,\text{cm}^2$ projected collection area, moving through a plasma of temperature $0.16\,\text{eV}$ at a velocity of $1\,\text{km/s}$ with a density of $10^4\,\text{cm}^{-3}$, $R \approx 10^7\,\Omega$. Analysis of the potential diagram shows that the electrometer measures

$$RI = \left[\mathbf{E}' \cdot \mathbf{d} + (V_1 - V_2) + (WF_2 - WF_1)\right] \Big/ \left[1 + (R_1/R) + (R_2/R)\right]$$

(Notice that the potential plotted is the electron potential energy, which is the negative of the normal potential in circuit analysis.) Clearly, to detect the full $\mathbf{E}' \cdot \mathbf{d}$ potential we need to have $R \gg R_j$, as well as to keep the error terms in the numerator small. This is quite easy with modern electronics, where input resistances of $10^{12}\,\Omega$ are easily available.

For systems with $|\mathbf{d}|$ small it is essential to control the asymmetries and surface properties by using spherical electrodes that are coated with a colloidal

suspension of carbon (Kelley, 1970) or are gold plated. Longer electrode base-lines can employ cylindrical sensors, which are easier to manufacture and inter-face with the mechanical structure. These systems overcome the signal-to-noise problem by increasing the signal.

Concerning recent ionospheric satellites, the very successful S3-2 and S3-3 and Viking satellites used spherical sensors mounted on triaxial or multiconductor electronic cables held outward by centrifugal force. Separations of 40–100 m tip to tip were obtained. The DE satellites used quasi-rigid cylindrical booms or single conductor wire booms with similar separation distances. In the latter case, the last few meters of the insulation covering the metallic boom was removed to make electrical contact with the plasma. Many ionospheric rockets have been flown in the past decade by various groups using primarily spherical sensors. For HF measurements, a preamp must be inside the sensor due to cable capacitance.

Motion of the spacecraft across the earth's magnetic field at velocity $\mathbf{V}_s$ creates an additional vector electric field contribution since in the moving frame the field $\mathbf{E}'$ is given by

$$\mathbf{E}' = \mathbf{E}_A + \mathbf{V}_s \times \mathbf{B}$$

where $\mathbf{E}_A$ is the desired ambient electric field. Subtraction of two vectors requires accurate knowledge of $\mathbf{V}_s$ and the vehicle attitude. The magnetic field itself is usually known quite well at ionospheric heights and is not a problem in carrying out the required vector subtraction.

The balloon-borne double-probe method is essentially identical except that the electronics and the system in general are much more sensitive to the requirement $(R \gg R_j)$. This is due to the very low charged particle density in the atmosphere and the correspondingly high value of R_j. What is surprising is that the horizontal electric field components at balloon heights (30 km) have anything at all to do with the ionosphere. In fact, a number of theoretical studies as well as the data itself show that ionospheric fields of large horizontal scale (± 100 km) map nearly unattenuated down to 30 km (Kelley and Mozer, 1975; Mozer and Serlin, 1969). Superpressure balloons have been used in the Southern Hemisphere, where very long-duration flights are possible, several months long in fact. Communication with these balloons is done via satellite links (Holzworth et al., 1984).

A.3.4 Electrostatic Wave Measurements

Almost all the waves discussed in this text are electrostatic in nature; that is, there are no associated magnetic field fluctuations. From Maxwell's equation,

$$\nabla \times \delta\mathbf{E} = -\partial(\delta B)/\partial t = 0$$

so $\delta\mathbf{E}$ may be derived from a potential

$$\delta\mathbf{E} = -\nabla(\delta\phi) \tag{A.34}$$

and thus the term *electrostatic* is used. This term does not imply a static phenomenon, however, since these waves can travel at quite high velocities and display high-frequency fluctuations. The linearized version of (A.34) is

$$\delta \mathbf{E} = -i\mathbf{k}(\delta\phi) \tag{A.35}$$

which shows that $\delta \mathbf{E}$ is parallel to the propagation vector.

For frequencies below either the ion plasma frequency or the lower hybrid frequency, whichever is lower, both ions and electrons participate in the response of the medium to wave electric fields. This implies further that there are density fluctuations $\delta n/n$ and a velocity fluctuation δ_v associated with the wave. Electrostatic waves may thus be detected by the density probes and by the drift meters described above.

Because of the motion of the spacecraft relative to the plasma, even pure spatial variations appear as temporal fluctuations in the vehicle frame. If the wave phase velocity in the plasma is much less than the relative velocity, then the frequency w in the spacecraft frame is just equal to $\mathbf{k} \cdot \mathbf{V}_R$. This assumption is almost always valid in the case of satellite measurements because of the large velocities ($\sim$7000 m/s) of the spacecraft and is often, but not always, valid for rockets as well. In the auroral zone, plasma drifts can easily exceed the component of rocket velocity of the vehicle and plasma perpendicular to $\mathbf{B}$. In this case, it is important to measure the quasi-dc electric field. In fact, the relative velocity of the vehicle and plasma perpendicular to $\mathbf{B}$ is $\mathbf{E}_R \times \mathbf{B}/B^2$, where $\mathbf{E}_R$ is the electric field measured directly with the rocket instruments in the rocket reference frame. If the wave frequency in the plasma frame is of the order of $\mathbf{k} \cdot \mathbf{V}_R$, the analysis is more complicated. Low-apogee rockets flown to study the equatorial and auroral electrojets fall in this category.

Although probes and radar systems both respond to irregularities in the plasma density, there is a fundamental difference which must be kept in mind in comparing results. As just discussed, the backscatter radar responds to irregularities with a unique wave number $\mathbf{k}$, which is nearly a three-dimensional delta function. A probe responds to any wave number for which $\mathbf{k} \cdot \mathbf{V}_R \neq 0$. Even at a given frequency ω' the wave number is not unique, since there are infinitely many wave numbers $\mathbf{k}$ such that $\omega' = \mathbf{k} \cdot \mathbf{V}_R$. The frequency response $S(\omega')$ of a density detector to a spectrum of pure irregularities $P_N(\mathbf{k})$ (zero frequency in the plasma frame) is given by

$$S(\omega') = (1/V_R) \iint P_N(k_1, k_2, \omega'/V_R) dk_1 dk_2 \tag{A.36}$$

where axis 3 is parallel to $\mathbf{V}_R$ and $\omega' = k_3 V_R$. As an example, consider the response of a detector to the isotropic power law spectrum of irregularities often discussed in relation to scintillations

$$P_N(\mathbf{k}) = \left(2^{1/2}\alpha N_0^2\right)\Big/\left(2\pi^2 k_0^2\right) \left\{1 + \left[k_0^{-4}\left(k_x^2 + k_y^2 + \alpha^2 k_z^2\right)\right]^2\right\}^{-1} \tag{A.37}$$

For a velocity perpendicular to the symmetry axis the double integration (Costa and Kelley, 1977) yields a spectrum which, for $\omega' > V_R k_0$, varies as ω^{-2}. Thus, a k^{-4} spectrum reduces to ω^{-2} for a one-dimensional measurement made by a spacecraft. More detailed discussions of this effect can be found in Costa (1978) and Fredericks and Coroniti (1976). The latter reference shows that in some cases a single measurement cannot be unambiguously interpreted in terms of ω and k if the Doppler shift frequency is comparable to ω. Comparison with theory is in principle most straightforward with computer simulations, since the one-dimensional spectrum can be found simply by sampling the computed density along a desired direction in the simulation. Such a comparison has been made by Kelley et al. (1987), as discussed in Chapter 4.

Since the density is a scalar quantity, no information is available on the angular distribution of irregularities. Thus, either theory or some other measurement techniques must be employed to relate the measured density fluctuation spectra to ambient spatial variations.

Although relative density detectors can be used to study irregularities, absolute measurements are important, since they pertain to zero-order conditions in the ionosphere and therefore to conditions that may be unstable to the production of irregularities. In cases where the plasma is stable at the operating wavelength, an incoherent scatter radar can be used to measure the background density structure and, in principle, long-wavelength irregularities. A notable exception is the Jicamarca radar, since during interesting events the system is usually dominated by 3 m irregularities due to instabilities.

Information on the propagation direction of the waves can be found from electric field measurements, since the electric field is a vector quantity. In an electrostatic wave, $\mathbf{k} \cdot \delta\mathbf{E} = 0$, and thus the direction of SE can be used to determine $\mathbf{k}$. In the case of a single plane wave the solution is straightforward, although there may still be an ambiguity in the sign of the phase velocity. In practice, a spectrum of irregularities exists which depends not only on $\mathbf{k}$ but also on the direction of propagation. Furthermore, the discussion surrounding (A.36) applies just as well to one-dimensional measurements of fluctuating electric fields (Fredericks and Coroniti, 1976). Thus, an inspired blending of theoretical understanding and other measurement results must be combined with electric field measurements to yield definitive interpretation of the angular dependence and the frequency spectra. Nonetheless, such measurements contain essential information and, in conjunction with radar or scintillation measurements, can be extremely valuable in understanding ionospheric instabilities.

If the wavelength of an electrostatic wave is shorter than the separation distance $\mathbf{d}$ between electrodes, then the full electric field potential $-\mathbf{E} \cdot \mathbf{d}$ is not measured. In fact, if an integral number of half-wavelengths separates the sensors, the voltage difference is zero. For a plane wave the voltage response is

$$V_s = \left[-\mathbf{E} \cdot \mathbf{d} \cos(\omega t - \theta) \sin(\mathbf{k} \cdot \mathbf{d}/2)\right] \Big/ (\mathbf{k} \cdot \mathbf{d}/2) \tag{A.38}$$

If $\mathbf{k} \cdot \mathbf{d} \ll 1$, this reduces to $\mathbf{E} \cdot \mathbf{d}$. For $\mathbf{k} \cdot \mathbf{d}/2$ large and a finite spread of wave numbers about some k_0, the sensor response is proportional to the wave potential ϕ_0 and not the wave electric field. Under certain conditions, these nulls can be used to determine the wavelength of the electrostatic wave since $\mathbf{d}$ is known (Temerin, 1978). Such information is invaluable for sorting out which wave mode causes a given fluctuation.

Simultaneous measurements of $\delta\mathbf{E}(\omega)$ or $\delta\mathbf{V}(\omega)$ and the density fluctuation spectrum $\delta n(\omega)/n$ can sometimes be used to determine the wave mode, since theory can be used to predict the relationship between the various components of the wave.

A.3.5 Barium Ion Cloud Measurements

Since the electric field is of crucial importance to the understanding of ionospheric dynamics, tracer techniques were developed in the 1960s to measure the flow velocity of the ionospheric plasma. The basic idea is to inject a small number of atoms into the medium under conditions such that the cloud is fully sunlit but observers on the ground are in darkness. For certain materials the sunlight both ionizes the material and makes it visible via a resonant scattering process. Barium vapor has proved to be the best material for this experiment and well over 100 releases have been carried out over the years at altitudes from 150 to 60,000 km.

To vaporize the barium metal, very high temperatures are needed, and a thermite reaction is used to attain the required heat of vaporization. As discussed in the text, small clouds are needed if the tracer aspect is important. "Small" in this case means that the height-integrated conductivity of the cloud must be less than that of the ionosphere. Following Haerendel et al. (1967), at F region altitudes the electric field is given by

$$\mathbf{E}_\perp = \frac{1 + \lambda^*}{2} B \left[\hat{B} \times \mathbf{V}_\perp + \frac{1}{k_i} (\mathbf{V}_\perp - \mathbf{U}_{n\perp}) + \frac{\lambda^* - 1}{\lambda^* + 1} \mathbf{U}_{n\perp} \times \mathbf{B} \right] \qquad (A.39)$$

where $\mathbf{V}_\perp$ is the velocity of the ion cloud perpendicular to $\mathbf{B}$, λ^* is the ratio of height-integrated Pedersen conductivities in the presence and in the absence of the cloud, k_i is the ratio of the gyration frequency to the collision frequencies of a barium ion, $\mathbf{U}_{n\perp}$ is the neutral wind velocity in the reference frame fixed to the earth, $\hat{B}$ is a unit vector parallel to the local magnetic field direction, and $\mathbf{E}$ and $\mathbf{E}_\perp$ represent the ionospheric electric field in a frame of reference fixed to the earth in the plane perpendicular to the local magnetic field direction. For $\lambda^* = 1$ and k_i large (F region altitudes) $\mathbf{V}_\perp$ is equal to $(\mathbf{E} \times \mathbf{B})/B^2$. The method has proved to be extremely valuable for measuring electric fields in the ionosphere. This is particularly true at low latitudes, where probe techniques and drift meters must contend with satellite velocities much in excess of the plasma velocity.

References

Babcock, H. D. (1923). A study of the green auroral line by the interference method. *Astrophys. J.* **57**, 209–221.

Bahcivan, H., Hysell, D. L., Larsen, M. F., and Pfaff, R. F. (2005). The 30 MHz imaging radar observations of auroral irregularities during the JOULE campaign. *J. Geophys. Res.* **110**, A05307, doi:10.1029/2004JA010975.

Baker, D. J., and Stair, A. T. (1988). Rocket measurements of the altitude distributions of the hydroxyl airglow. *Physica Scripta* **37**, 611.

Bates, D. R. (1981). The green light of the night sky. *Planet. Space Sci.* **29**, 1061–1067.

Bauer, S. J., and Nagy, A. F. (1975). Ionospheric direct measurement techniques. *Proc. IEEE* **63**, 1.

Born, M., and Wolf, E. (1999). *Principles of Optics: Electromagnetic Theory of Propagation Interference and Diffraction of Light*. 7th ed., Cambridge University Press, Cambridge, ISBN 0521642221.

Bowhill, S. A. (1961). Statistics of a radio wave diffracted by a random ionosphere. *J. Res. Natl. Bur. Stand., Sect. D* **65**, 275.

Bowles, K. L. (1958). Observations of vertical incidence scatter from the ionosphere at 41 Mc/sec. *Phys. Rev. Lett.* **1**, 454.

Budden, K. G. (1965). The amplitude fluctuations of the radio wave scattered from a thick ionospheric layer with weak irregularities. *J. Atmos. Terr. Phys.* **27**, 155.

Costa, E. (1978). *Aspects of the Linear and Nonlinear Development of Equatorial Spread F with Application to Ionospheric Scintillation*. Ph.D. Thesis, Cornell University, Ithaca, New York.

Costa, E., and Kelley, M. C. (1977). Ionospheric scintillation calculations based on in situ irregularity spectra. *Radio Sci.* **12**, 797.

Cronyn, W. M. (1970). The analysis of radio scattering and space probe observations of small scale structure in the interplanetary medium. *Astrophys. J.* **161**, 755.

Fahleson, U. V. (1967). Theory of electric field measurements conducted in the magnetosphere with electric probes. *Space Sci. Rev.* **7**, 238.

Farley, D. T. (1979). The ionospheric plasma. *Solar Syst. Plasma Phys.* **3**.

Fejer, B., and Kelley, M. C. (1980). Ionospheric irregularities. *Rev. Geophys. Space Res.* **18**, 401.

Fredericks, R. W., and Coroniti, F. V. (1976). Ambiguities in the deduction of rest frame fluctuation spectra from spectra computed in moving frames. *J. Geophys. Res.* **81**, 5591.

Gordon, W. E. (1958). Incoherent scattering of radio waves by free electrons with application to space exploration by radar. *Proc. TRE* **46**, 1824.

Haerendel, G., Lust, R., and Rieger, E. (1967). Motion of artificial ion clouds in the upper atmosphere. *Planet. Space Sci.* **15**, 1.

Hagen, J. B., and Behnke, R. A. (1976). Detection of the electron component of the spectrum in incoherent scatter of radio waves by the ionosphere. *J. Geophys. Res.* **81**, 3441.

Hagen, J. B., and Hsu, P. Y. (1974). The structure of the protonosphere above Arecibo. *J. Geophys. Res.* **79**, 4269.

Hanuise, C., and Crochet, M. (1978). Oblique HF radar studies of plasma instabilities in the equatorial electrojet in Africa. *J. Atmos. Terr. Phys.* **40**, 49.

Hecht, E. (1998). *Optics*. 3rd ed., Addison-Wesley, Reading, MA, ISBN 0201838877.

Hernandez, G. (1986). *Fabry-Perot Interferometers*. Cambridge University Press, Cambridge, ISBN 0521322383.

Hewish, A. (1952). The diffraction of galactic radio waves as a method of investigating the irregular structure of the ionosphere. *Proc. R. Soc. London, Ser. A*. **214**, 494.

Holzworth, R. H., Onsager, T., and Powell, S. (1984). Planetary-scale variability of the fair-weather vertical electric field in the stratosphere. *Phys. Rev. Lett.* **53**, 1398.

Hysell, D. L., Larsen, M. F., and Zhou, Q. H. (2004). Common volume coherent and incoherent scatter radar observations of mid-latitude sporadic E-layers and QP echoes. *Ann. Geophys.* **22**, 3277–3290.

Kelley, M. C. (1970). *Auroral Zone Electric Field Measurements on Sounding Rockets*. Ph.D. thesis, Physics Department, University of California at Berkeley.

Kelley, M. C., and Mozer, F. S. (1975). Simultaneous measurement of the horizontal components of the earth's electric field in the atmosphere and in the ionosphere. *J. Geophys. Res.* **80**, 3275.

Kelley, M. C., Seyler, C. E., and Zargham, S. (1987). Collisional interchange instability. 2. A comparison of the numerical simulations with the in situ experimental data. *J. Geophys. Res.* **92**, 10,089.

Klein, M. V., and Furtak, T. E. (1986). *Optics*. 2nd ed., John Wiley and Sons, New York, ISBN 0471872970.

Kudeki, E., Fejer, B. G., Farley, D. T., and Ierkic, H. M. (1981). Interferometer studies of equatorial F region irregularities and drifts. *Geophys. Res. Lett.* **8**, 377.

Lovelace, R. E., Salpeter, E. E., Sharp, L. E., and Harris, D. E. (1970). Analysis of observations of interplanetary scintillations. *Astrophys. J.* **159**, 1047.

Makela, J. J., and Kelley, M. C. (2003). Using the 630.0-nm nightglow emission as a surrogate for the ionospheric Pedersen conductivity. *J. Geophys. Res.* **108**(A6), 1253, doi:10.1029/2003JA009894.

Makela, J. J., Kelley, M. C., González, S. A., Aponte, A., and McCoy, R. P. (2001). Ionospheric topography maps using multiple-wavelength all-sky images. *J. Geophys. Res.* **106**(A12), 29,161–29,174.

Measures, R. M. (1992). *Laser Remote Sensing: Fundamentals and Applications*. Krieger, Florida.

Meinel, A. B. (1950). OH emission bands in the spectrum of the night sky. *Astrophys. J.* **111**, 555–564.

Mercier, R. P. (1962). Diffraction by a screen causing large random fluctuations. *Proc. Cambridge Philos. Soc.* **58**, 382.

Meriwether, J. W., Taylor, M. J., and Slanger, T. G. (2004). *Self-Assessment Review on Passive Optics Aeronomy*. Report to the CEDAR Science Steering Committee and to the National Science Foundation.

Miller, C. A. (1996). *On Gravity Waves and the Electrodynamics of the Mid-Latitude Ionosphere*. Ph.D. thesis, Cornell University, Ithaca, NY.

Mott-Smith, H., and Langmuir, I. (1926). The theory of collections in gaseous discharges. *Phys. Rev.* **28**, 727.

Mozer, F. S. (1973). Analysis of techniques for measuring DC and AC electric fields in the magnetosphere. *Space Sci. Rev.* **14**, 272.

Mozer, F. S., and Serlin, R. (1969). Magnetospheric electric field measurements with balloons. *J. Geophys. Res.* **74**, 4739.

Providakes, J. F., Swartz, W. E., Farley, D. T., and Fejer, B. G. (1983). First VHF auroral radar interferometer observations. *Geophys. Res. Lett.* **10**, 401.

Rishbeth, H., and Garriott, O. K. (1969). *Introduction to Ionospheric Physics*. Academic Press, New York.

Rufenach, C. L. (1971). A radio scintillation method of estimating the small-scale structure in the ionosphere. *J. Atmos. Terr. Phys.* **33**, 1941.

Rufenach, C. L. (1972). Power law wave number spectrum deduced from ionospheric scintillation observations. *J. Geophys. Res.* **77**, 4761.

Rufenach, C. L. (1975). Ionospheric scintillation by a random phase screen: Spectral approach. *Radio Sci.* **10**, 155.

Saleh, B. E. A., and Teich, M. C. (1991). *Fundamentals of Photonics*. John Wiley and Sons, New York, ISBN 0471839655.

Salpeter, E. E. (1967). Interplanetary scintillation. I. Theory. *Astrophys. J.* **147**, 433.

Skinner, W. R., Hays, P. B., and Abreu, V. J. (1987). Optimization of a triple etalon interferometer. *Appl. Opt.* **26**, 2817.

Swenson, G. R., and Gardner, C. S. (1998). Analytic models for the responses of the mesospheric OH* and Na layers to atmospheric gravity waves. *J. Geophys. Res.* **103**, 6271–6294.

Swenson, G. R., and Mende, S. B. (1994). OH emission and gravity waves (including a breaking wave) in all-sky imagery from Bear Lake, UT. *Geophys. Res. Lett.* **21**, 2239–2242.

Szuszczewicz, E. P., and Takacs, P. Z. (1979). Magnetosheath effects on cylindrical Langmuir probes. *Phys. Fluids* **22**, 2424.

Tatarskii, V. I. (1961). *Wave Propagation in a Turbulent Medium*. Dover, New York.

Taylor, M. J., Swenson, G. R., and Taylor, V. (1995). Height measurements of the OI (557.7 nm) gravity wave structure over the Hawaiian Islands during ALOHA-93. *Geophys. Res. Lett.* **22**, 2881–2884.

Temerin, M. (1978). The polarization, frequency, and wavelengths of high-latitude turbulence. *J. Geophys. Res.* **83**, 2609.

Tsunoda, R. T., Perreault, P. D., and Hodges, J. C. (1976). Azimuthal distribution of HF slant E region echoes and its relationship to the polar cap electric field. *J. Geophys. Res.* **81**, 3834.

Wagner, L. S. (1962). Diffraction by a thin phase-changing ionospheric layer with applications to radio star scintillation. *J. Geophys. Res.* **67**, 4195.

Wayne, R. P. (1991). *Chemistry of Atmospheres: An Introduction to the Chemistry of the Atmospheres of Earth, the Planets, and Their Satellites*. Oxford University Press.

Wright, J. W., and Pitteway, M. L. V. (1979). Real-time data acquisition and interpretation capabilities of the dynasonde. 2. Determination and magnetoionic mode and echo location using a small spaced receiving array. *Radio Sci.* **14**, 827.